Optics & Laser Technology 201 (2026) 115284

Contents lists available at ScienceDirect

Optics and Laser Technology

journal homepage: www.elsevier.com/locate/optlastec

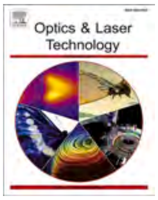

Investigating the effect of different axial oscillation waveforms in laser fusion cutting☆

Matteo Busatto [a,*], Julia Meyer [b], Leonardo Caprio [a], Davide Gandolfi [c], Barbara Previtali [a]

[a] Department of Mechanical Engineering, Politecnico di Milano, Via La Masa 1, 20156 Milan, Italy
[b] Fraunhofer Institute for Material and Beam Technology IWS, Winterbergstr. 28, 01277 Dresden, Germany
[c] Adige S.P.A., BLM GROUP, Via per Barco 11, 38056 Levico Terme TN, Italy

ARTICLE INFO

Keywords:
Laser cutting
Beam shaping
Axial oscillations
Waveforms

ABSTRACT

Laser processing systems provide elevated flexibility in dynamically shaping the laser beam in both space and time. Scientific literature indicates that such techniques represent promising solutions for improving both part quality and process productivity. However, methodological investigations for the processing of high thickness metal sheets have not been extensively reported. The wide range of possibilities enabled by novel beam-shaping approaches has yet to be systematically explored. The present work aims to study the effect of axial oscillations (*i. e.* along the beam propagation axis) in laser fusion cutting. By leveraging an analytical model, the power density distribution generated by different oscillation waveforms was explored. An experimental set up was developed to include a deformable mirror with the capability of generating high frequency modifications of the beam focal position, thus enabling experiments with axial oscillations in the 100–1500 Hz range. Successively, experiments were performed to demonstrate the improvements achievable in terms of part quality and productivity. While existing literature has primarily focused on dynamic beam shaping employing harmonic oscillations, this study explores the impact of various oscillation waveforms, including sinusoidal, triangular, square, ramp-up, and ramp-down patterns. Hence, the analytical model predicted the time-averaged laser power distribution within the process zone for the different oscillation waveforms. The use of axial oscillations, superimposed to the cutting-direction, was investigated during the processing of 20 mm thick AISI304. Experimental results demonstrate notable improvements in process performance, either by reducing burr defects in *iso*-productivity conditions or by increasing the speed whilst maintaining equivalent part quality.

1. Introduction

Today, laser fusion cutting of metal materials stands out as one of the key technologies in the sheet processing field. Conventionally, material separation relies on the combined action of a high-intensity laser beam and a coaxial high-pressure gas jet operating near the workpiece. Specifically, in fusion cutting, the laser provides the thermal energy required to melt the material, while an inert assist gas removes the molten metal from the kerf [1,2]. Since its introduction into the metalworking industry, research has been directed toward enhancing laser cutting performance, with particular attention to improving cut-edge quality and increasing process productivity. Scientific investigation demonstrated that the performance of laser cutting is strongly influenced by both the characteristics of the laser beam (such as wavelength, power, polarization, temporal emission, beam size, and intensity distribution) and the selection of process parameters, namely focal position, assist gas type and pressure, and cutting speed, specific to the material and thickness being processed [3,4]. As a result, considerable attention has been devoted to investigating how these factors and their interactions affect cut quality, productivity, and overall process performance.

To date, various strategies have been explored to enhance laser cutting performance by tailoring laser beam characteristics, commonly referred to as Beam Shaping (BS) methods [5]. These strategies include modifications of the emission wavelength [6,7], polarization state [8,9], temporal emission characteristics [10,11], and spatial intensity distribution [12,13]. Among these, recent advancements in laser cutting

---

☆ This article is part of a special issue entitled: ‘LIM 2025’ published in Optics and Laser Technology.

* Corresponding author.

E-mail addresses: matteo.busatto@polimi.it (M. Busatto), julia.meyer@iws.fraunhofer.de (J. Meyer), leonardo.caprio@polimi.it (L. Caprio), davide.gandolfi@blmgroup.it (D. Gandolfi), barbara.previtali@polimi.it (B. Previtali).

https://doi.org/10.1016/j.optlastec.2026.115284
Received 10 October 2025; Received in revised form 22 December 2025; Accepted 18 February 2026

Nomenclature

Symbol	Name (Units)
(x, y, z)	Geometrical coordinates in three-dimensional space, [mm]
(x_0, y_0, z_0)	Laser focal position coordinates in three-dimensional space, [mm]
$I(x, y, z)$	Laser intensity distribution in three-dimensional space, $\left[\mathrm{W}\cdot\mathrm{mm}^{-2}\right]$
I_{pk}	Peak laser intensity, $\left[\mathrm{W}\cdot\mathrm{mm}^{-2}\right]$
$\overline{I(x, y, z)}$	Time-averaged laser intensity distribution in three-dimensional space, $\left[\mathrm{W}\cdot\mathrm{mm}^{-2}\right]$
I_{pk}^{static}	Peak laser intensity in static conditions, $\left[\mathrm{W}\cdot\mathrm{mm}^{-2}\right]$
I_{norm}	Normalized laser intensity distribution in three-dimensional space, [−]
P	Laser power, [kW]
λ	Laser source emission wavelength, [nm]
BPP	Laser source Beam Parameter Product, [mm·mrad]
z_R	Rayleigh length, [mm]
w_0	Beam waist radius (at z_0 axial position), [mm]
$w(z)$	Beam radius (at z axial position), [mm]
f_{col}	Collimator focal length, [mm]
f_{foc}	Focusing lens focal length, [mm]
d_{core}	Laser source fiber core diameter, [mm]
v	Laser cutting process speed, [mm/min]
Pr	Assistant gas pressure, [bar]
FP	Laser beam focal position with respect to the head nozzle, [mm]
SOD	Stand-off distance between the head nozzle and workpiece surface, [mm]
d_{nozzle}	Nozzle diameter, [mm]
t	Material thickness, [mm]
R_z	Mean peak to valley height roughness profile value, [µm]
h	Mean burr height value, [mm]
HAZ	Heat affected zone, [mm]
$\mu(w_{kerf})$	Average kerf width, [mm]
$\sigma(w_{kerf})$	Kerf width variation (unevenness), [mm]
u	Kerf perpendicularity, [mm]
θ_{front}	Front incident angle, [deg]
$z'(t)$	Time-dependent axial position coordinate, [mm]
$S_z(t)$	Axial oscillation component, [mm]
A	Axial oscillation amplitude, [mm]
ω	Axial angular oscillation frequency, $\left[\mathrm{rad\,s}^{-2}\right]$
T	Axial oscillation period, [s]
ϕ	Phase shift contribution, [rad]
SNW	Sinusoidal waveform pattern
SQW	Square waveform pattern
TNW	Triangular waveform pattern
RUW	Ramp-up waveform pattern
RDW	Ramp-down waveform pattern

techniques utilizing spatial Dynamic Beam Shaping (DBS) methods have demonstrated substantial improvements in processing speed and part quality. These techniques rely on the high-speed motion of laser beam, superimposed to the cutting direction. Laser oscillations around the kerf enable to shape the interaction zone into an arbitrary geometry while preserving the beam intensity distribution [14,15]. Several studies have investigated the influence of laser beam oscillations in the XY plane (*i.e.* along the travel direction of the beam and transversally to it) on process performance using different dynamic beam shaping technologies. Goppold *et al.* examined the effects on the part quality of various sinusoidal oscillations during the cutting of thick stainless steel plates, employing both a high-dynamic scanner system [16,17] and a tip-tilt piezo platform mirror [18]. Levichev *et al.* reported notable improvements in the part quality of 12 mm thick mild and stainless steel using sinusoidal linear oscillations along the cutting direction [19,20]. Additionally, Kardan *et al.* implemented thermal monitoring and high-speed imaging to evaluate cutting process dynamics, specifically investigating how oscillation amplitude and frequency affect workpiece temperature and melt flow behaviour [21,22]. Significant improvements in process performance have also been reported for beam oscillation applied along the laser propagation direction (Z-axis). Gropp *et al.* and Okada *et al.* were among the first to show that the quick adaptation of the laser beam focal position is expected to enable an increase in processing speed and improvement in the quality of laser material processing [23,24]. Initially, vertical oscillations of the laser beam were achieved through electromechanical or pneumatic devices, which had strict constraints regarding the positioning range and oscillation frequency [25,26]. Recently, alternative solution that enable oscillations of the laser focal plane along the beam propagation direction were developed based on novel Fast Focusing Mirrors (FFMs). These are mirrors that can rapidly adjust their surface shape to change the divergence and, hence, the focus position of an incident light beam. A detailed analysis of the working principle of a FFM was first presented by Bottner *et al.* [27], while the integration of such solution into a commercial processing head for cutting and welding application was demonstrated by Jahn *et al.* [28]. In their study, a 3 kW fiber laser source was employed to process 10 mm thick stainless steel, resulting in a 60% increase in cutting speed through the application of sinusoidal axial oscillations. A further study by Herwig *et al.* addressed the impact of harmonic axial oscillations on the productivity of fusion cutting process across a variety of materials and thicknesses [29]. Their findings revealed increases in processing speed for stainless steel, mild steel and aluminum alloy materials of various thicknesses, utilizing a 3 kW laser power.

In this context, the present work explores the effect of dynamic axial oscillations on laser fusion cutting, aiming to enhance process performance in terms of both productivity and part quality. Whereas existing literature has primarily concentrated on dynamic beam shaping based on harmonic sinusoidal oscillations, this study examines the influence of multiple oscillation waveform patterns to identify those that provide the greatest improvement relative to static operating conditions. In addition to conventional sinusoidal (SNW) oscillations, the waveforms considered include triangular (TNW), square (SQW), ramp-up (RUW), and ramp-down (RDW) patterns. An analytical model was initially developed to evaluate the time-average laser power distribution within the process zone under both static and dynamic conditions. Furthermore, the effect of axial oscillations, superimposed to the cutting direction, on process performance was experimentally investigated for 20 mm thick AISI304 stainless steel material.

2. Modelling

As highlighted by Mahrle and Beyer [30], controlled laser beam oscillations govern the energy delivered to the material, significantly influencing melt pool dynamics and, ultimately, material separation [31,32]. Accordingly, an analytical model was developed to evaluate the time-averaged laser intensity distribution within the process zone under both static and dynamic conditions. For the first time, the present model accounts for the spatial and temporal motion of the laser beam, considering not only oscillation amplitude and frequency but also different oscillation patterns.

The spatial intensity distribution under dynamic beam shaping conditions strictly depends on the laser beam motion, as well as the intensity distribution of the incident beam. For a conventional laser beam operating in static conditions, its intensity distribution can be well-approximated by a Gaussian function. Considering an overall laser power P [W], a Rayleigh length z_R [mm] and a beam waist radius w_0 [mm] in axial position z_0 [mm], the analytic expression of its intensity distribution in 3D space, centered in (x_0, y_0, z_0) coordinates, is defined by the well-known formula [33]:

$$I(x,y,z) = I_{pk}(z)\cdot exp\left[-2\cdot\frac{(x-x_0)^2+(y-y_0)^2}{w(z)^2}\right] \tag{1}$$

where the laser peak intensity $I_{pk}(z)$ [W mm^{-2}] and beam radius $w(z)$ [mm] at position z [mm] can be computed as:

$$I_{pk}(z) = \frac{2\cdot P}{\pi\cdot w(z)^2} \tag{2}$$

$$w(z) = w_0\cdot\sqrt{1+\frac{(z-z'(t))^2}{z_R^2}} \tag{3}$$

and, in turn, the beam waist radius w_0 [mm] at the focus and Rayleigh length z_R [mm] are defined in terms of the beam parameter product BPP [mm mrad] and the full divergence angle of the laser beam θ [rad]:

$$w_0 = \frac{BPP}{\theta} \tag{4}$$

$$z_R = \frac{w_0^2}{BPP} \tag{5}$$

However, to account for the dynamic motion of the laser beam along its propagation direction (Z-axis), the time-dependent position coordinate $z'(t)$ [mm] may be expressed as follows:

$$z'(t) = z_0 + S_z(t) \tag{6}$$

where z_0 [mm] denote the initial position coordinate, and $S_z(t)$ [mm] represent the oscillation component that account for the axial moving trajectory of the beam focus. The explicit expression of the time-dependent oscillation term varies according to the selected motion function. For harmonic oscillations, this may be simply described by a sinusoidal function. Here, the parameter A [mm] denotes the oscillation amplitude, ω [rad s^{-1}] is the angular frequency and ϕ [rad] represents the phase shift contributions, which is set to zero for a properly chosen time reference:

$$S_z(t) = A\cdot sin(\omega\cdot t+\phi) \tag{7}$$

The angular frequency ω [rad s^{-2}] is related to the oscillation frequency f [Hz], or the oscillation period T [s] as:

$$\omega = 2\pi\cdot f = \frac{2\pi}{T} \tag{8}$$

A schematic representation of time-domain sinusoidal oscillations along the laser beam propagation direction is reported in Fig. 1, while its analytical expression is reported in Equation (9).

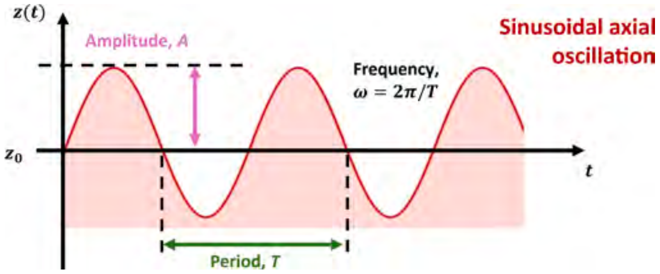

Fig. 1. Time-domain representation of sinusoidal oscillations along the z direction.

Although existing literature has primarily focused on dynamic beam shaping employing harmonic sinusoidal (SNW) oscillations, alternative waveforms such as triangular (TNW), square (SQW), ramp-up (RUW), and ramp-down (RDW) can also be utilized. Schematic representations of the waveform patterns are reported in Fig. 2, while the analytical expressions are here provided [34]:

$$SNW(t) = A\cdot sin(\omega\cdot t) \tag{9}$$

$$TNW(t) = \frac{8\cdot A}{\pi^2}\cdot\sum_{n=1}^{n=N}\left\{\frac{(-1)^n}{(2n\pm1)^2}\cdot sin[\omega\cdot(2n-1)\cdot t]\right\} \tag{10}$$

$$SQW(t) = \frac{4\cdot A}{\pi}\cdot\sum_{n=1}^{n=N}\left\{\frac{1}{2n-1}\cdot sin[\omega\cdot(2n-1)\cdot t]\right\} \tag{11}$$

$$RUW(t) = \frac{A}{2}+\frac{2\cdot A}{\pi}\cdot\sum_{n=1}^{n=N}\left\{\frac{(-1)^{n+1}}{n}\cdot sin[\omega\cdot n\cdot t]\right\} \tag{12}$$

$$RDW(t) = \frac{A}{2}-\frac{2\cdot A}{\pi}\cdot\sum_{n=1}^{n=N}\left\{\frac{1}{n}\cdot sin[\omega\cdot n\cdot t]\right\} \tag{13}$$

In theory, the exact waveform representation is obtained by evaluating the infinite Fourier series ($N\rightarrow\infty$). In practical implementations, however, the series must be truncated to a finite number of terms (N), resulting in an approximate reconstruction of the target waveform. The fidelity of this approximation improves with increasing N, as higher-order harmonics contribute to a more accurate reproduction of the waveform shape. Nevertheless, the achievable value of N is inherently limited by the dynamic response of the actuation system employed to generate the oscillations. Specifically, the maximum realizable harmonic order depends on the device bandwidth and its capability to sustain the required displacement amplitude at the given oscillation frequency. Consequently, the selection of N represents a trade-off between waveform accuracy and the physical constraints of the actuation hardware, and it is strongly influenced by the waveform type, operating frequency, and amplitude.

The time-averaged spatial intensity distribution $\bar{I}(x,y,z)$ [W mm^{-2}] under varying operating conditions can be calculated as the mean value of the previous expression, Equation (1), over a single oscillation period T [s], as:

$$\bar{I}(x,y,z) = \frac{1}{T}\cdot\int_0^T I(x,y,z,t)\cdot dt \tag{14}$$

For better comparison, the intensity distributions associated with the different oscillation patterns are normalized with respect to the peak intensity of the static condition $I_{pk,static}$ [mm], according to the following expression:

$$I_{norm} = \frac{\bar{I}(x,y,z)}{I_{pk,static}} \tag{15}$$

3. Material and methods

3.1. Material

This study investigates the fusion cutting process of 20 mm thick stainless steel AISI304 material. This was selected due to its industrial relevance in the metal-working industry. The nominal chemical composition is reported in Table 1 and was declared to be in accordance with BS EN 10088–3:2023 standard by the supplier [35].

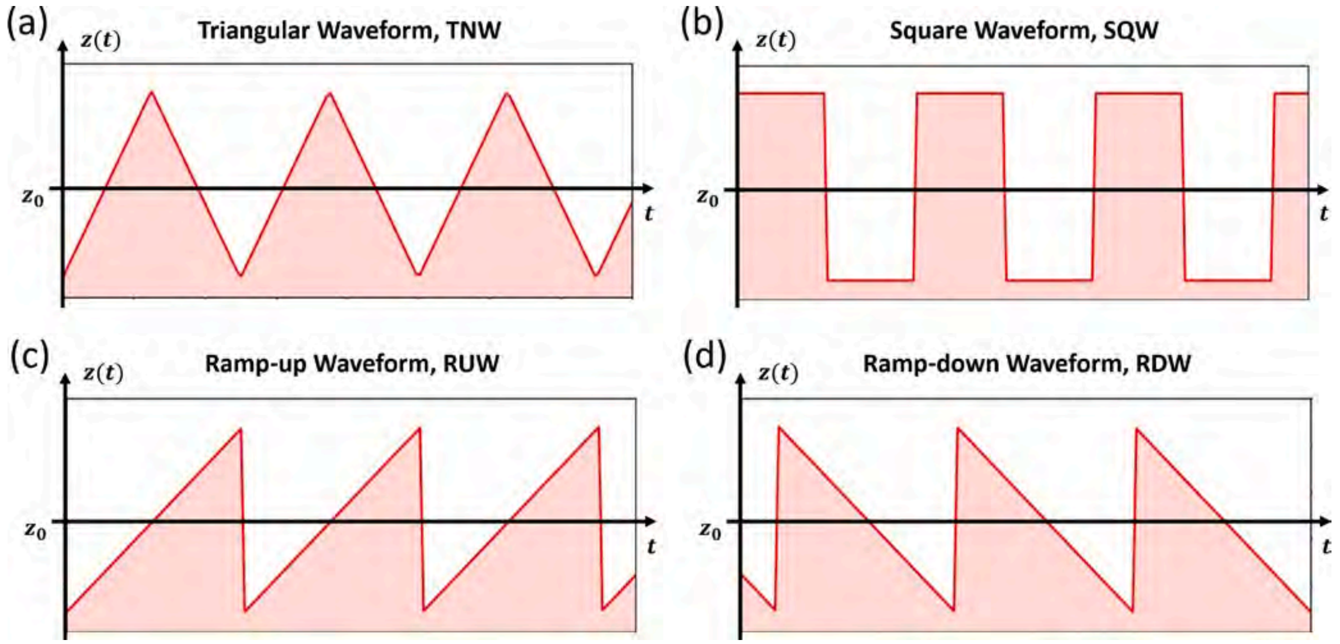

Fig. 2. Time-domain representations of different oscillation waveform patterns: (a) triangular TNW, (b) square SQW and (c) ramp-up RUW and (d) ramp-down RDW.

Table 1
Nominal chemical composition of AISI304 stainless steel in wt% [35].

Element	C	Si	Mn	P	S	Cr	Ni	Mo	Fe
wt (%)	0.02	0.52	1.50	0.01	0.01	17.30	11.40	2.46	Bal.

3.2. Laser cutting system

The cutting experiments were performed on a customized version of a commercial Arnold 3D double-head cutting system (Fraunhofer IWS institute, Dresden, Germany). An industrial high-power multi-mode fiber laser source that can deliver an approximately Gaussian beam profile with a nominal power up to $P_{nom} = 12000$ W at a central emission wavelength of $\lambda = 1080$ nm (MFMC12000M, Maxphotonics Co., Ltd, Shenzhen, Guangdong, China) was employed to cut the material. The transport fiber is a graded-index optical fiber having a core diameter of $d_{core} = 0.05$ mm and is coupled to a customized version of the Precitec HPSSL (Precitec GmbH & Co., Gaggenau, Germany) cutting head with a

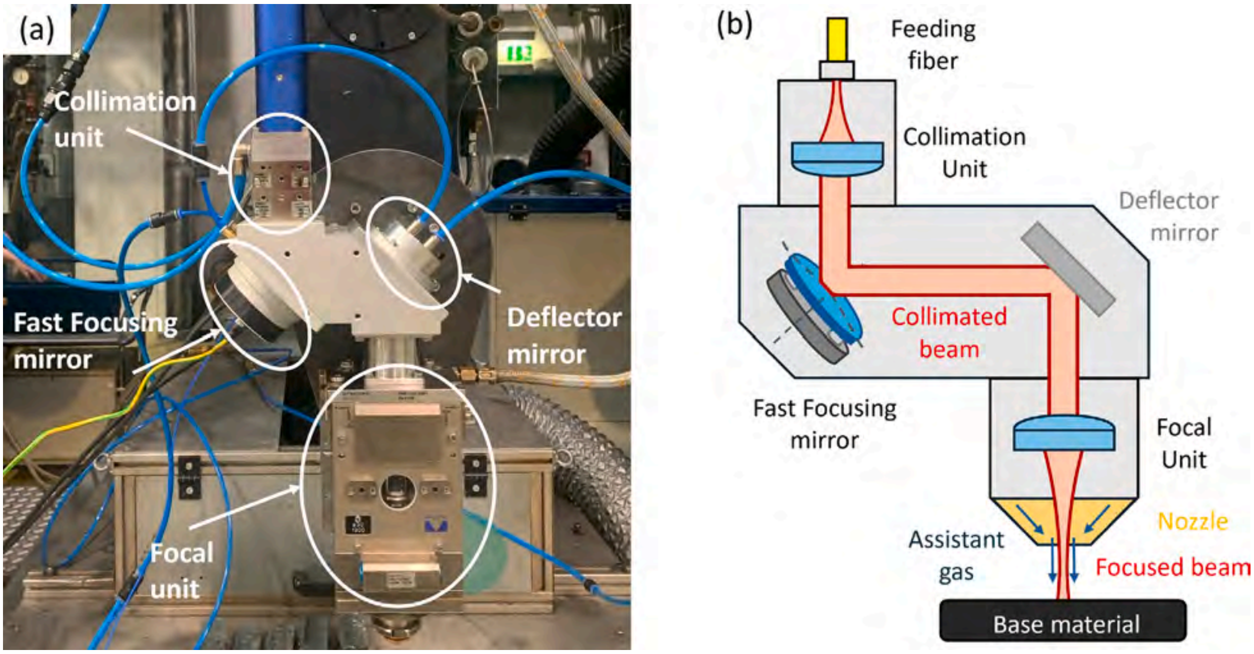

Fig. 3. (a) Photo and (b) Schematic representation of the novel laser cutting system to enable high-frequency oscillations along the beam propagation (axial) direction. Customized version of the Precitec HPSSL cutting head equipped with a Fast Focusing Mirror (Zwobble system, ROBUST AO GmbH, Jena, Germany).

collimation and a focusing lens of $f_{col} = 100$ mm and $f_{foc} = 200$ mm focal length, respectively. This optical configuration results in a theoretical beam waist at the focal position that can be computed as follows [36]:

$$w_0 = \frac{d_{core}}{2} \cdot \frac{f_{foc}}{f_{col}} = 0.05\,\text{mm} \quad (16)$$

Furthermore, dynamic beam shaping functionality was achieved by integrating a Fast Focusing Mirror (FFM) into the conventional Precitec HPSSL cutting head, as schematically represented in Fig. 3. Specifically, a ROBUST AO [37] Zwobble scanner (ROBUST AO GmbH, Jena, Germany) was selected and integrated into the cutting head to enable high-frequency oscillations along the beam propagation direction (axial oscillations). A photograph and schematic representation of the novel cutting head to enable high-frequency oscillations along the beam propagation direction are shown in Fig. 3.

The scanning system consisted of a single Fast-Focusing Mirror (FFM), *i.e.* a deformable mirror capable of rapidly adjusting its surface shape. By modifying the mirror surface curvature, the divergence of the incoming collimated laser beam can be controlled, thereby enabling precise adjustment of the focal position after the focusing optics. This configuration allows for the generation of fast axial oscillations of the laser beam along the propagation direction. With the employed scanning system and optical path, axial oscillations along the laser beam propagation direction reached a maximum amplitude of 15 mm and a maximum frequency of 1500 Hz. However, the maximum amplitude is frequency-dependent: when the system was set to operate with a 15 mm amplitude, the maximum operating frequency achievable in such condition for the different waveforms were 1000 Hz for sinusoidal and triangular patterns, 500 Hz for ramp-up and ramp-down waveforms and 100 Hz for the square waveform.

The laser beam caustic and power density distribution of the novel cutting system under static operating conditions were characterized using a Primes MicroSpotMonitor (PRIMES GmbH, Pfungstadt, Germany), in accordance with the ISO 11146 standard. The measured beam characteristics were consistent with both the specifications provided by the laser manufacturer and the theoretical predictions obtained from the modelling section. In particular, the experimentally measured beam waist radius and Rayleigh length closely matched the theoretical values. A summary of the measured laser system specifications, which show good agreement with the theoretical parameters, is reported in Table 2.

While the Primes MicroSpotMonitor provides a reliable characterization of the laser beam under static conditions, an Ophir BeamWatch (MKS Instruments Photonics Solutions Division, Wilmington, Massachusetts, United States) device was used to quantify key intensity distribution parameters (such as beam radius and Rayleigh length) under dynamic processing conditions. Prior to integrating the fast focusing mirror into the industrial laser cutting head, real-time measurements of the laser beam during axial oscillation were conducted. Practical testing and verification of these parameters are essential to ensure that the analytical model accurately reflects the actual beam behaviour during dynamic operation.

Table 2
Laser system specifications of the self-developed experimental set up.

Parameters	Values
Laser power, P_{nom} [W]	12 000
Wavelength, λ [nm]	1080
Beam Parameter Product, BPP [mm mrad]	1.62
Full divergence angle, θ [mrad]	65.69
Collimation length, f_{col} [mm]	100
Focal length, f_{foc} [mm]	200
Feeding fibre core diameter, d_{core} [mm]	0.05
Beam waist radius, w_0 [mm]	0.05

3.3. Experimental plan

This study investigates the effect of axial oscillations on laser fusion cutting performance through analytical modelling and experimental analysis. In particular, the effect of different axial oscillation waveform patterns on processing speed and part quality is evaluated for 20 mm thick stainless steel AISI304, with the aim of identifying the pattern that delivers the greatest improvement in process performance.

An overview of the process parameters (namely laser power, cutting speed, assist gas pressure, focal position and stand-off distance) applied for cutting this material in static conditions is provided in Table 3. The fixed parameters, as well as those used for the static reference condition, correspond to the settings commonly adopted in industrial practice for cutting with a static beam. These parameters were provided by the machine manufacturer and validated in this study through preliminary experimental investigations. They represent operating conditions that maximize the nominal cutting speed while still ensuring an acceptable level of part quality, evaluated in terms of burr formation and surface roughness.

Subsequently, an experimental plan was designed to assess the influence of various laser oscillation waveform patterns on productivity and part quality of 20 mm thick stainless steel AISI304. The sample geometry consisted of a 20 mm x 100 mm rectangle with a straight, incomplete cut line through the sample centre to assess cutting front and kerf geometry, following the approach of Bocksrocker *et al.* [38]. Based on preliminary investigations and consistent with findings from previous studies [28], significant improvements in process performances were observed for focal positions located near the center of the material and for oscillation amplitudes spanning the entire thickness. Accordingly, two focal positions were selected, at 6 mm and 10 mm below the material surface, while the peak-to-peak oscillation amplitude was fixed at the maximum value of 15 mm enabled by the oscillating system. To assess the influence of oscillation frequency, cutting experiments were performed at three representative frequency levels (100 Hz, 500 Hz and 1000 Hz) covering the entire usable oscillation range. The selection of these values was constrained by the dynamic limits of the mirror system, as previously noted. Hence, at the 15 mm oscillation amplitude, employed sinusoidal and triangular patterns could be performed up to a maximum frequency of 1000 Hz, whereas ramp-up and ramp-down waveforms were limited to 500 Hz, and the square waveform to only 100 Hz.

To evaluate the process productivity under dynamic beam shaping conditions, the cutting speed was incrementally increased from the value obtained in the static reference condition (0.7 m/min) up to 1.0 m/min, resulting in a total of six speed levels. To ensure statistical significance, two replicates were carried out for each processing condition.

Table 3
Experimental plan for 20 mm thick AISI304 laser fusion cutting process under static and dynamic axial oscillations.

Process parameters	Values	
Fixed parameters		
Laser power, P [W]	6000	
Assist gas	N_2	
Gas pressure, pr [bar]	20	
Nozzle diameter, d_{nozzle} [mm]	3.0	
Stand-off Distance, SOD [mm]	0.7	
	Reference	**Axial oscillations**
Oscillation patterns	Static	Sinusoidal; Triangular; Square; Ramp-up; Ramp-down
Focal position, FP [mm]	−12	−6; −10
Oscillation amplitude, A [mm]	n.a.	15
Oscillation frequency, f [Hz]	n.a.	100; 500; 1000
Cutting speed, v [m/min]	0.70	0.70; 0.80; 0.85; 0.90; 0.95; 1.00

A stand-off distance of 0.7 mm was maintained for all experiments, together with the maximum assist-gas pressure allowed by the cutting machine (approximately 20 bar), in order to promote efficient melt ejection. A nozzle with a diameter of 3 mm was used, as typically required for processing thick materials to guarantee sufficient gas flow and stable kerf evacuation. The laser power was fixed at 6000 W, which was the maximum level admissible for safe operation of the deflector mirror. The fixed and variable process parameters are outlined in Table 3.

3.3.1. Characterisation equipment and procedures

The samples obtained from experimental investigations were visually inspected and grouped under the following three categorical conditions:

- Successful Cut: the molten material is ejected, leading to complete material separation.
- Plasma Cut: unstable laser cutting process conditions may induce plasma formation, resulting in complete material separation but with low cut-edge quality [39].
- Loss of Cut: the molten material is not ejected from the kerf but resolidified, preventing material separation.

Representative optical microscope images of these conditions are reported in Fig. 4: (a) Successful Cut and (b) Plasma Cut, both showing the cut kerf surface in a side view, while (c) Loss of Cut, shown in a top view. Loss of Cut conditions are indicated in red, while Plasma Cut and Successful Cut conditions are indicated in yellow and green, respectively.

For successful cutting conditions, process productivity was evaluated based on the maximum cutting speed achievable while maintaining acceptable cut quality [40]. As discussed by Pacher *et al.*, part quality in laser cutting is traditionally assessed using several criteria, including burr attachment, kerf width, surface roughness, heat affected zone and presence of burns on the cut edge [41]. Although the relative importance of these indicators varies depending on the final application of the processed components, several studies have shown that the burr height [42] and the surface roughness profile [43] are the most significant indicators of overall cut quality and are among the most widely adopted metrics in industrial laser cutting of high-thickness metal materials. Accordingly, in the present study, part quality was primarily assessed through measurements of cut-edge roughness profile R_z and burr height h, the latter representing the most critical parameter for 20 mm thick stainless steel. For each axial oscillation waveform pattern, the process conditions that minimized burr formation and roughness were identified. Under these selected conditions, the kerf geometry [44] and cutting front shape [45] were further characterized by the average kerf width $\mu(w_{kerf})$, kerf with deviation (unevenness) $\sigma(w_{kerf})$, kerf perpendicularity u, and the cutting front incident angle θ_{front}. In addition, the Heat-Affected Zone (HAZ) was systematically evaluated by measuring its width at multiple locations along the cut edge, as it represents a key indicator of the thermal impact of the process and reflects the extent of microstructural and metallurgical alterations induced by the laser-material interaction [46]. These parameters provide complementary information on the cutting performance and were therefore evaluated under the process conditions that yielded the lowest burr height, *i.e.*, after optimization of the cut quality in terms of roughness and burr formation.

The Keyence VHX digital microscope (Keyence corporation, Osaka, Japan) was employed for high-resolution imaging of the samples cut-edges, while the burr height defect was extracted through a Python image processing algorithm. The coloured microscope image of the cut-edge profile was first converted into a grayscale image and then to a binary matrix by applying a thresholding operation based on pixel intensity. The top and bottom sample edges were identified and the matrix image was rotated to compensate for misalignment. Subsequently, the difference between the two profile edges was computed and by subtracting the material thickness, a reliable estimation of the burr defect h along the entire sample profile was identified. An example is reported in Fig. 5a.

The surface roughness of the cut edge was evaluated in accordance with the UNI EN ISO 9013:2017 and ISO 4287:1997 [Rev. ISO 21920–2:2021] standards [47,48]. According to these standards, surface roughness of laser-cut parts is characterized using the R_{z5} parameter, which is defined as the average of the five highest peak-to-valley distances measured along the cut edge profile. Measurements were performed using a Jenoptik Waveline W20 profilometer (Jenoptik AG, Jena, Thüringen, Germany) equipped with an TKU-300 feeler and a 5 μm stylus tip. In compliance with the reference standards, the acquired primary profile for each sample is filtered by a frequency filter with a 0.8 mm cut-off wavelength. The roughness profile was measured at three different positions along the cut-edge surface, as represented schematically in Fig. 5b: at the centre of the material and 1 mm above and below the top and bottom surface respectively. Three measurements were taken at each position, and the mean and standard deviation values were computed.

Furthermore, kerf width was evaluated from metallographic cross-sections transverse to the cut direction (Fig. 5c). Samples were sectioned using a high-precision manual abrasive cut-off machine (MECATOME ST 3010, Presi, France) to minimize thermal and mechanical damage, then mounted, ground, and polished using a semi-automatic polishing system (MECATECH 300 SPC, Presi, France). Polished cross-sections were imaged with a Keyence VHX digital microscope (Keyence, Osaka, Japan). Kerf width profiles, $w_{kerf}(z)$, were extracted from high-resolution images using an image-processing approach similar to that applied for burr height. The colour images were converted to grayscale and then binarized using intensity thresholding. The left and right kerf edges were identified, and any

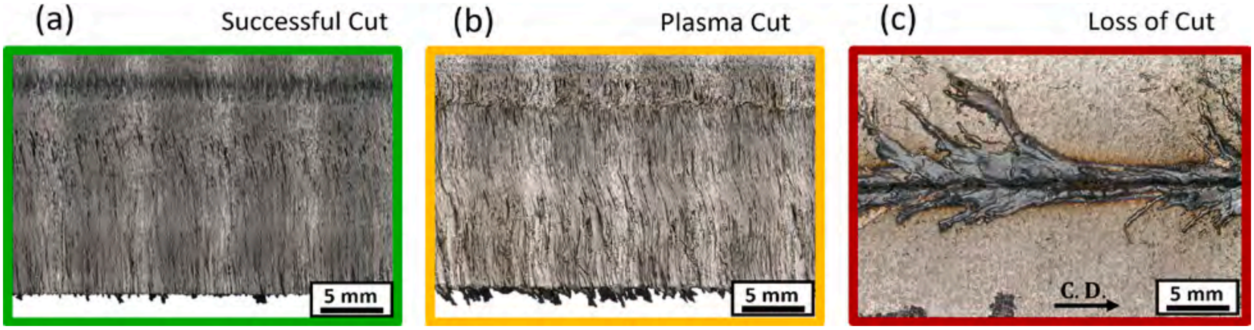

Fig. 4. Qualitative cutting results for 20 mm thick AISI304 stainless steel: (a) Successful Cut and (b) Plasma Cut, both showing the kerf surface in a side view, while (c) Loss of Cut, shown in a top view. Loss of Cut conditions are indicated in red, while Plasma Cut and Successful Cut conditions are indicated in yellow and green, respectively.

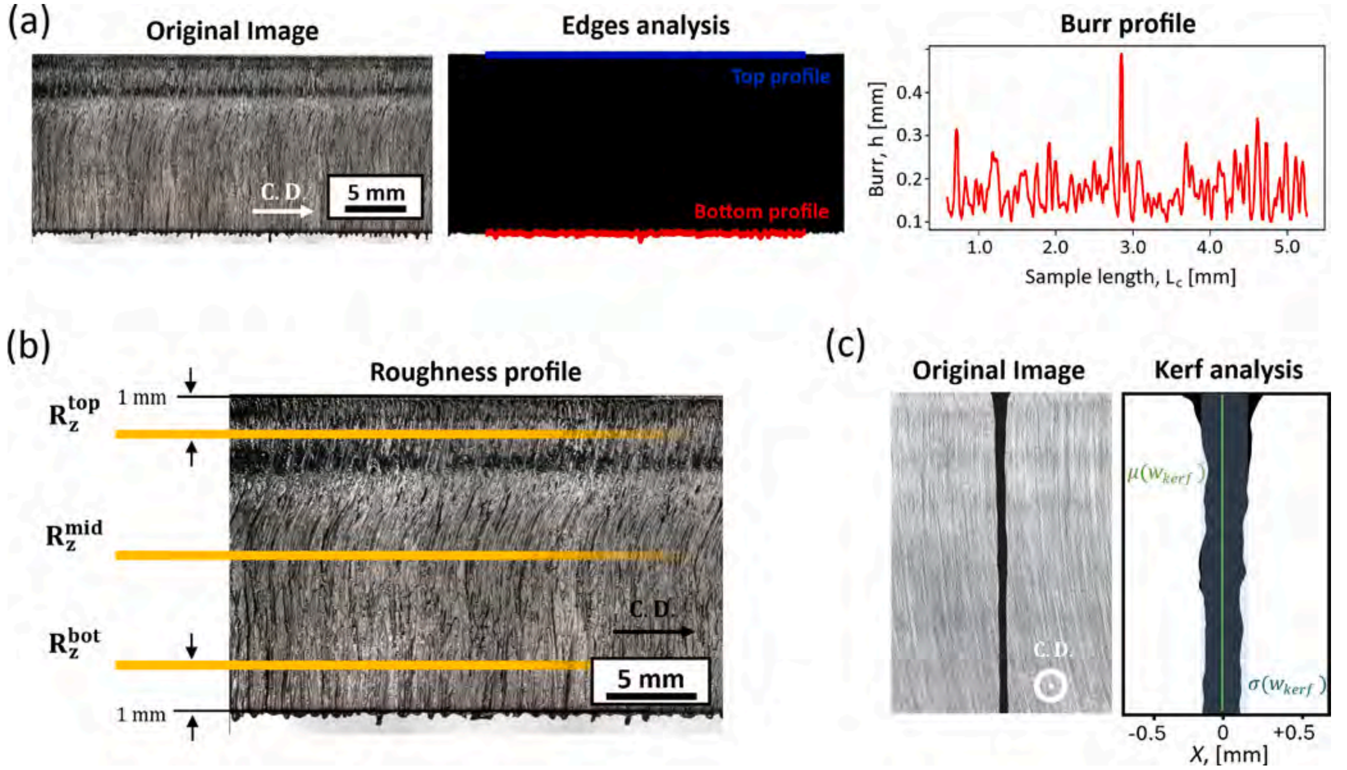

Fig. 5. (a) Burr estimation procedure: Original microscope image; Binary image; Detection of the top and bottom cut-edge profiles and rotation for misalignment compensation; Extraction of the burr profile along the sample length. (b) Surface roughness measurement. Three different positions along the cut-edge surface: the center of the material and 1 mm above and below the top and bottom surface. (c) Kerf width analysis: Original microscope image of the sample cross-section; extraction of the kerf width profile to compute the average kerf width $\mu(w_{kerf})$, standard deviation $\sigma(w_{kerf})$, and kerf perpendicularity u.

misalignment was corrected by image rotation. Distances between opposing edges were computed along the full material thickness to obtain the kerf width profile. The mean $\mu(w_{kerf})$ and standard deviation $\sigma(w_{kerf})$ were calculated to quantify average width and variability. Kerf perpendicularity, u, was determined according to EN ISO 9013:2017. The inclination of the cutting front θ_{front} was evaluated through image analysis of metallographic sections prepared along the cutting direction.

Finally, the thermal impact of the process was evaluated through measurements of the heat-affected-zone (HAZ). Cross-sections transverse to the cutting direction were mechanically polished using abrasive papers and polishing cloths with diamond suspensions down to a final grit size of 1 μm, and subsequently subjected to chemical etching. The etching solution consisted of 1 mL of nitric acid (65% concentration), 1 mL of hydrochloric acid (37% concentration), and 1 mL of distilled water [49]. The samples were immersed in the etchant for 1 min. This chemical etching procedure revealed the geometry of the heat-affected-zone, which was then acquired by optical microscopy. The HAZ was systematically evaluated by measuring its width at multiple locations along the cut edge, equally spaced at 2 mm intervals along the material thickness, resulting in a total of eleven measurement positions.

4. Results

4.1. *Time-average spatial intensity distribution*

Based on the analytical model presented in section 2 and the available experimental setup described in section 3.2, the time-averaged laser intensity distribution was computed as the integral over one oscillation period of the Gaussian beam intensity profile undergoing various axial oscillation waveforms, namely sinusoidal SNW, triangular TNW, ramp-up RUW and square SQW. The following parameters were used in the analysis: laser power $P = 6000$ W, emission wavelength $\lambda = 1080$ nm, beam parameter product $BPP = 1.62$ mm mrad, full divergence angle $\theta = 65.69$ mrad, beam waist radius at the focal position $w_0 = 0.05$ mm, and oscillation amplitude $A = 15$ mm. As previously mentioned, oscillations are constrained by the mirror dynamics, with square wave patterns reaching a maximum frequency of $f = 100$ Hz, which was selected for the evaluation of the time-averaged spatial intensity distribution to ensure proper implementation of all waveform patterns.

A visual comparison between the (a) static intensity distribution and the time-averaged spatial intensity distributions obtained under various axial oscillation waveforms: (b) sinusoidal SNW, (c) triangular TNW, (d) ramp-up RUW and (e) square SQW, all with fixed amplitude of $A = 15$ mm and frequency $f = 100$ Hz are shown in Fig. 6. It is evident that axial oscillations have a significant influence on the laser power distribution. Specifically, for all oscillation patterns, the visible reduction in peak intensity is accompanied by an enlargement of the axial range over which a more uniform and homogeneous intensity distribution is sustained, extending across the entire oscillation range for sinusoidal, triangular, ramp-up and ramp-down waveforms. While triangular and ramps oscillation patterns yield beam radius and peak intensity distributions similar to those of sinusoidal oscillation, the square waveform produces a distinct profile. In particular, it generates an intensity distribution along the axial propagation direction that closely resembles the effect of diffractive optical elements designed to produce a double focal point [50,51]. In this case, the highest peak intensity occurs at the inversion point positions ($z = \pm A$).

For a quantitative analysis, the laser beam spot size and peak intensity distribution along the axial direction were determined through numerical calculations. Fig. 7 presents: (a) the laser beam radius $w(z)$ and (b) the peak intensity, $I_{pk}(z)$, as a function of axial position for different oscillation patterns. Fixed oscillation amplitude of $A = 15$ mm and frequency $f = 100$ Hz. These theoretical predictions are in good agreement with the values obtained from dynamic measurements of key

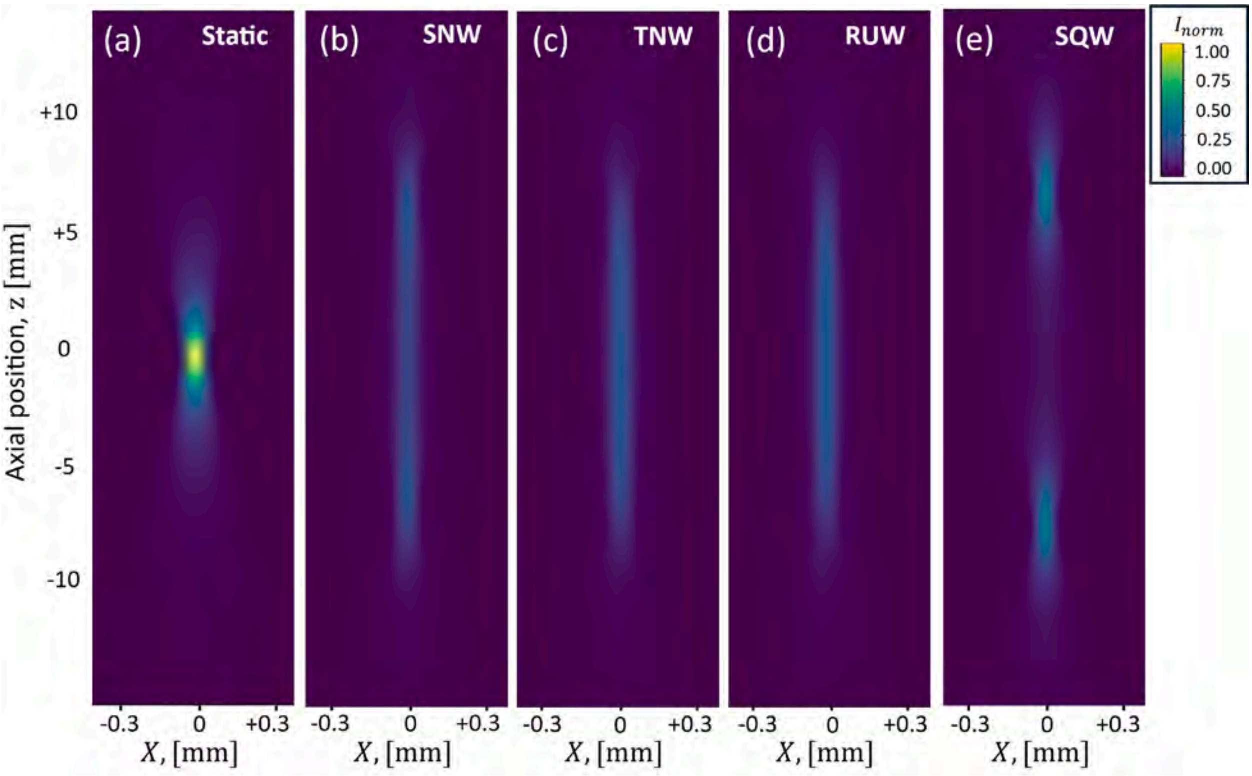

Fig. 6. Visual comparison between: (a) static intensity distribution and time-averaged intensity distributions obtained under various axial oscillation waveforms: (b) sinusoidal SNW, (c) triangular TNW, (d) ramp-up RUW and (e) square SQW. The following parameters were used in the analysis: laser power $P = 6000$ W, emission wavelength $\lambda = 1080$ nm, beam parameter product $BPP = 1.62$ mm mrad, full divergence angle $\theta = 65.69$ mrad, beam waist radius at the focal position $w_0 = 0.05$ mm, oscillation amplitude $A = 15$ mm and frequency $f = 100$ Hz.

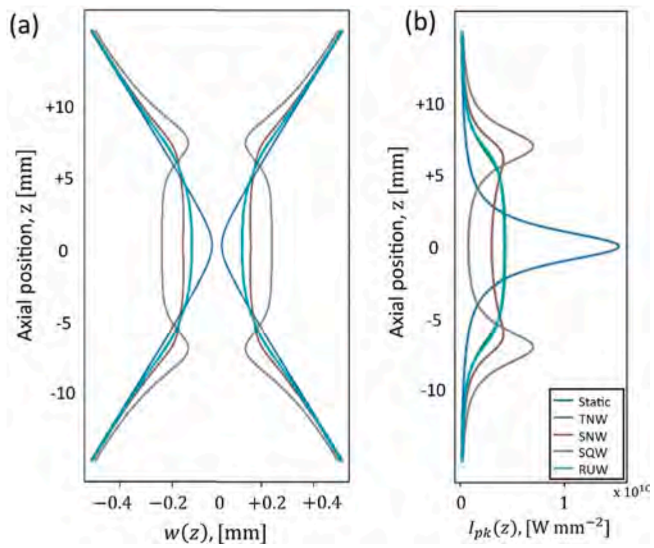

Fig. 7. (a) Laser beam radius $w(z)$ [mm] and (b) peak intensity $I_{pk}(z)$ [W mm^{-2}] along laser propagation direction for different waveforms: Static, Sinusoidal SNW, Triangular TNW, Square SQW and Ramp-up RUW. The following parameters were used in the analysis: laser power $P = 6000$ W, emission wavelength $\lambda = 1080$ nm, beam parameter product $BPP = 1.62$ mm mrad, full divergence angle $\theta = 65.69$ mrad, beam waist radius at the focal position $w_0 = 0.05$ mm, oscillation amplitude $A = 15$ mm and frequency $f = 100$ Hz.

intensity distribution parameters performed with an Ophir BeamWatch (MKS Instruments Photonics Solutions Division, Wilmington, Massachusetts, United States). The results of this experimental characterization confirm that the measured parameters closely match the values predicted by the analytical model, demonstrating its accuracy in estimating the laser intensity distribution under dynamic conditions.

Axial oscillations lead to a reduction in laser peak intensity, as observable in Fig. 6 and confirmed in Fig. 7b, while simultaneously enlarging the overall beam dimension at the focal position, which is maintained over a broader axial range, as shown in Fig. 7a. For sinusoidal oscillations, the beam waist radius increases from 0.05 mm under static conditions to approximately 0.2 mm, and this expanded radius is preserved across the entire oscillation range, from –7 mm to +7 mm around the focal plane. As a consequence, the Rayleigh length increases substantially, from 1.54 mm under static conditions to about 11 mm under axial sinusoidal oscillations. Regarding the intensity distribution, numerical calculations reported in Fig. 7b confirm the visual observations from Fig. 6. Under sinusoidal oscillations, the peak intensity diminishes, but correspondingly, the high-intensity region widens, resulting in a nearly uniform intensity level across the oscillation range. A slightly higher intensity peak can be observed at the extremes of the oscillation range ($z = \pm A$), which can be attributed to the presence of turning points, where the oscillatory velocity of the laser beam momentarily reaches zero due to the sinusoidal scan pattern. Beyond the oscillation range, however, the beam radius follows the same behaviour as in static conditions, maintaining a constant divergence, peak intensity and beam dimensions. For triangular and ramp oscillations, the intensity distribution behaves in a similar way, with a slightly higher intensity in the oscillation center position and without the localized peaks at the turning points. This is due to the sharper directional changes characteristics of triangular and ramp-up oscillations compared to sinusoidal ones. In addition, the beam waist expands up to 0.18 mm (slightly lower than in the sinusoidal case) yet still remains stable across the full oscillation range, with the Rayleigh length reaching a similar value of approximately 11 mm. It is worth noting that triangular and ramp oscillations exhibit nearly identical simulated behaviour. This outcome is explained by the fact that the simulations consider oscillations along axial direction for a stationary beam (translational speed set to zero). Consequently, differences between triangular, ramp-up and ramp-down oscillations do not manifest under these conditions but become relevant once beam translation is introduced, as will be demonstrated in the experimental results presented in the following sections. Finally, for square oscillations, the beam exhibits a markedly different behaviour: at the theoretical focal position, the beam radius reaches a value of about 0.25 mm, which is maintained only over a shorter axial distance compared to the oscillation range. At the extremes of the oscillation range, the beam radius decreases to approximately 0.15 mm while reaching the highest peak intensity. This behaviour resembles that of a laser beam with two distinct focal positions, leading to a more complex intensity distribution within the process zone.

The more homogeneous intensity distribution along the laser beam propagation direction, combined with the increased Rayleigh length, promotes a more uniform absorption of laser power throughout the thickness of the material, as discussed by Mahrle *et al.* [52,53]. Axial oscillations allow shaping of the interaction zone between the laser and the material, which is expected to improve process efficiency and enable higher processing speeds. Moreover, the modified geometry of the intensity profile has been shown to significant influence the resulting cutting kerf [54], potentially facilitating better coupling of the assist gas to the kerf and thereby improving gas flow. This enhanced flow can promote more efficient removal of molten material, thereby positively affecting the quality of the cut samples as shown in the simulations of the laser-gas interaction using CFD analysis performed by Borkmann *et al.* [55].

These effects, namely the higher processing speeds, along with improved part quality, will be experimentally verified in the following sections. In particular, the influence of different oscillation waveform patterns at varying frequencies will be investigated, with the corresponding results presented and discussed in detail. The current model for estimating the time-averaged laser intensity distribution focuses solely on the spatial distribution of laser intensity and does not account for oscillation frequency. However, when combined with the cutting motion, oscillation frequency may have a significant impact on overall process performance. Therefore, its effect will be evaluated experimentally.

4.2. *Experimental results*

The samples resulting from the experimental plan presented in section 3.3 were visually inspected and classified as Loss of Cut, Plasma Cut, or Successful Cut conditions (see Fig. 4). The resulting feasibility maps for the two distinct focal positions, (a) *FP* = -6 mm and (b) *FP* = -10 mm, are presented in Fig. 8, where Loss of Cut, Plasma Cut, and Successful Cut conditions are indicated in red, yellow, and green, respectively. The maps are shown as a function of cutting speed (*v* = 0.70 m/min, 0.80 m/min, 0.85 m/min, 0.90 m/min and 0.95 m/min) and oscillation frequency (*f* = 100 Hz, 500 Hz and 1000 Hz) for different waveform patterns: sinusoidal (SNW), triangular (TNW), square (SQW), ramp-up (RUW), and ramp-down (RDW). The oscillation amplitude was fixed at *A* = 15 mm.

According to Fig. 8, laser fusion cutting with dynamic beam shaping enables a notable increase in processing speed across a range of conditions, with maximum values reaching 0.90 m/min compared to the static reference of 0.70 m/min, corresponding to a 28% increase. Specifically, for sinusoidal oscillations, a cutting speed comparable to the reference (0.70 m/min) was achieved at *FP* = -10 mm and *f* = 100 Hz, while higher speeds of up to 0.80 m/min were reached at the same focal position for *f* = 500 Hz and *f* = 1000 Hz. At *FP* = -6 mm, speeds of 0.80 m/min were observed for *f* = 100 Hz and *f* = 500 Hz, with a maximum

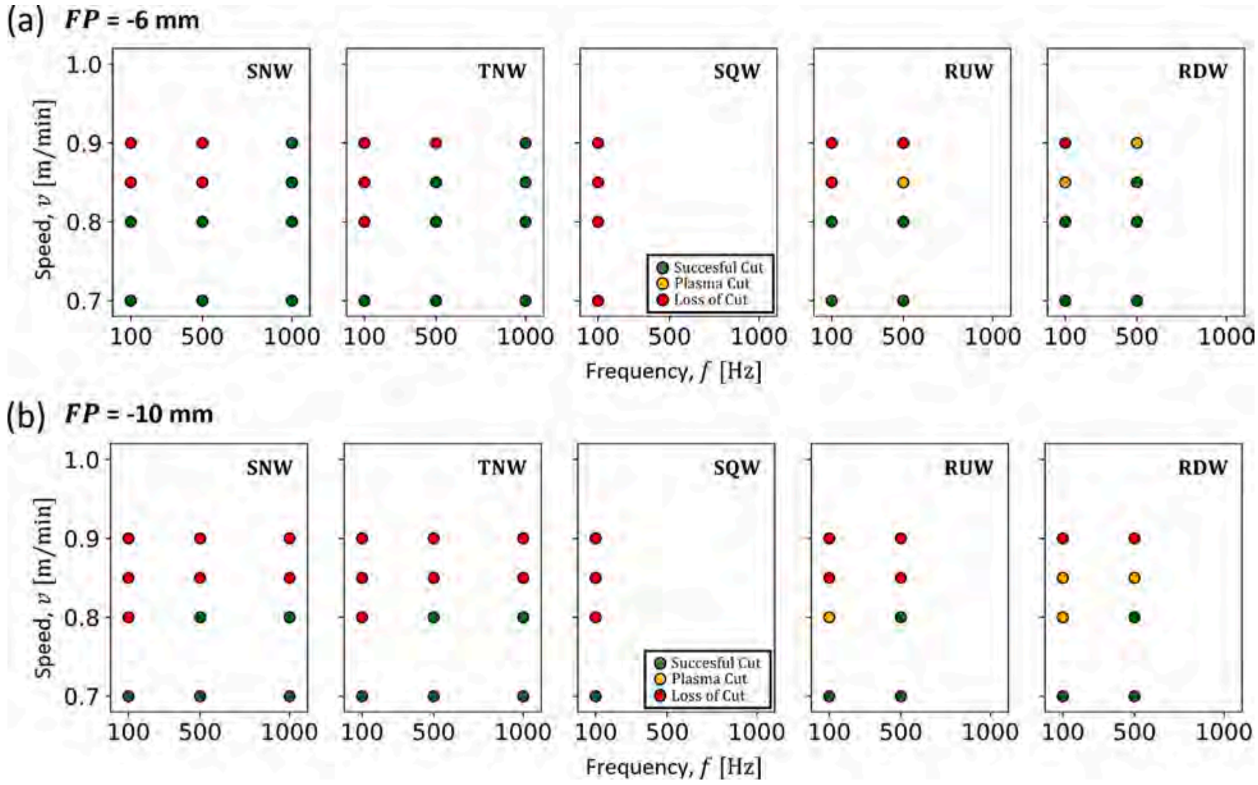

Fig. 8. Feasibility maps for the processing of 20 mm thick AISI304 stainless steel material. Two distinct focal positions, (a) *FP* = -6 mm and (b) *FP* = -10 mm. Loss of Cut, Plasma Cut, and Successful Cut conditions are indicated in red, yellow, and green, respectively. Different combinations of processing speed (*v* = 0.70 m/min, 0.80 m/min, 0.85 m/min, 0.90 m/min and 0.95 m/min) and oscillation frequency (*f* = 100 Hz, 500 Hz and 1000 Hz) for different waveform patterns: sinusoidal (SNW), triangular (TNW), square (SQW), ramp-up (RUW), and ramp-down (RDW). The oscillation amplitude was fixed at *A* = 15 mm.

increase to 0.90 m/min at $f = 1000$ Hz. This clearly indicates that increasing oscillation frequency enhances cutting speed for sinusoidal oscillations, particularly at focal position *FP* = -6 mm. The triangular oscillation pattern exhibited a similar trend to sinusoidal oscillations. At *FP* = -10 mm, the reference speed of 0.70 m/min was matched at $f =$ 100 Hz, while speeds up to 0.80 m/min were obtained for $f = 500$ Hz and $f = 1000$ Hz. At *FP* = -6 mm, the cutting speed reached 0.80 m/min at $f = 100$ Hz and increased to 0.85 m/min and 0.90 m/min for $f = 500$ Hz and $f = 1000$ Hz, respectively. This confirms that triangular and sinusoidal oscillations similarly influence cutting speed, with higher frequencies promoting faster processing, particularly at focal position *FP* = -6 mm. For the square oscillation pattern, cutting performance was more limited. No successful cuts were achieved at *FP* = -6 mm, while the reference speed of 0.70 m/min was matched at *FP* = -10 mm and $f =$ 100 Hz. The ramp-up waveform resulted in moderate speed increases. At *FP* = -6 mm, speeds up to 0.80 m/min were achieved for $f = 100$ Hz and $f = 500$ Hz, whereas at *FP* = -10 mm, 0.80 m/min was obtained only at f = 500 Hz, with the reference speed of 0.70 m/min maintained at $f =$ 100 Hz. Finally, ramp-down oscillations exhibited a similar behaviour. At *FP* = -10 mm, a cutting speed of 0.80 m/min was obtained at $f = 500$ Hz, decreasing to 0.70 m/min at $f = 100$ Hz. At *FP* = -6 mm, the speed was 0.80 m/min at $f = 100$ Hz, increasing to 0.85 m/min at $f = 500$ Hz. Overall, ramp-down oscillations enabled higher cutting speeds than ramp-up, although the improvements remained less pronounced than those achieved with sinusoidal and triangular oscillations.

Overall, dynamic beam shaping through axial oscillations demonstrates a substantial enhancement of cutting performance compared to the static reference case in terms of maximum achievable processing

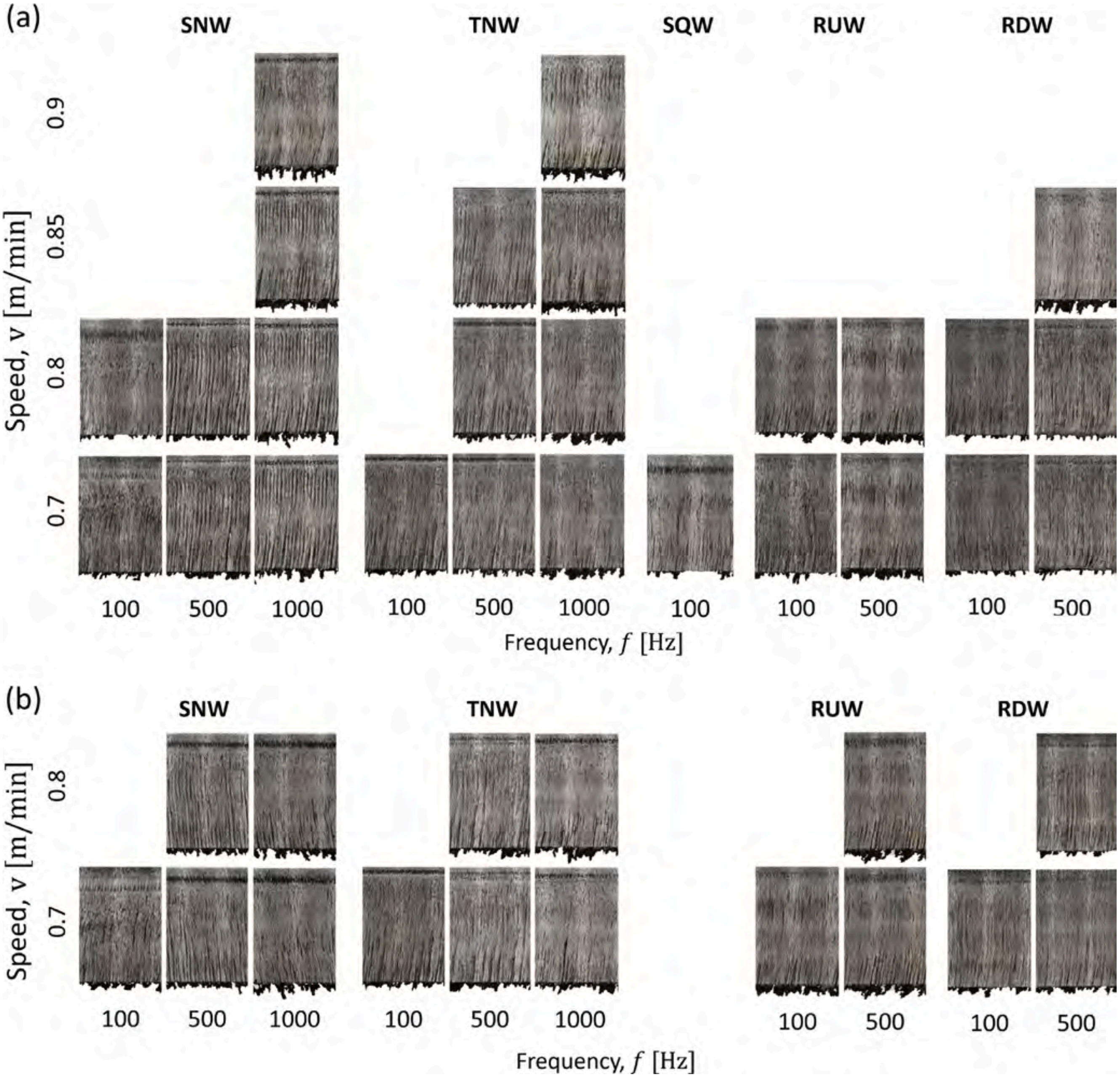

Fig. 9. Microscope images of the 20 mm thick AISI304 stainless steel samples cut-edges retrieved from experimental investigation for (a) *FP* = -6 mm and (b) *FP* = -10 mm. Different combinations of processing speed ($v = 0.70$ m/min, 0.80 m/min, 0.85 m/min and 0.90 m/min) and oscillation frequency ($f = 100$ Hz, 500 Hz and 1000 Hz) for different waveform patterns: sinusoidal (SNW), triangular (TNW), square (SQW), ramp-up (RUW), and ramp-down (RDW). The oscillation amplitude was fixed at $A = 15$ mm.

speed. However, the effect depends strongly on the oscillation waveform, frequency, and focal position, with sinusoidal and triangular patterns providing the most consistent speed improvements (up to 0.90 m/min).

Furthermore, the samples obtained under the various processing conditions were qualitatively assessed via observation of the cut-edge profiles. The corresponding optical microscope images are shown in Fig. 9, specifically for (a) *FP* = -6 mm and (b) *FP* = -10 mm. The images are presented as a function of processing speed (v = 0.70 m/min, 0.80 m/min, 0.85 m/min and 0.90 m/min) and oscillation frequency (f = 100 Hz, 500 Hz and 1000 Hz) for different waveform patterns: sinusoidal (SNW), triangular (TNW), square (SQW), ramp-up (RUW), and ramp-down (RDW). The oscillation amplitude was fixed at A = 15 mm. Visual inspection of the cut-edge samples indicates that dynamic beam shaping through axial oscillations strongly influences both processing speed and burr defect formation. While higher oscillation frequencies (especially at *FP* = -6 mm) lead to increased cutting speeds, they are also associated with larger burr heights.

To provide a quantitatively assessment of the processed samples' quality, burr height and roughness profile were evaluated as the key indicators commonly adopted in both industrial and scientific contexts for assessing part quality in laser cutting [41]. The measurement procedures for burr height and roughness followed the methodology described in section 3.3.1. Pronounced variations in burr height were observed across the different processing conditions, with oscillation pattern, frequency, focal position, and cutting speed all influencing burr formation. In contrast, surface roughness was affected primarily by the transition from static to dynamic (axial oscillation) cutting conditions. Once oscillations were introduced, no statistically significant variations in roughness were detected as a result of changes in focal position, oscillation frequency, or cutting speed within the same waveform pattern. Specifically, the R_z values under different axial oscillation conditions remained comparable to the static reference at the upper measurement position, with values around 0.04 mm. For the static condition, roughness increased significantly at the middle and lower positions, reaching approximately 0.20 mm and 0.27 mm, respectively. Under dynamic conditions, roughness at these two positions also increased relative to the top surface but remained consistently lower than in the static case, with values in the range of approximately 0.05——0.10 mm at the middle position and 0.10–0.15 mm at the lower position.

Furthermore, the burr height results are presented graphically in Fig. 10, with (a) showing results for *FP* = -6 mm and (b) *FP* = -10 mm. Mean values and one standard deviation error bars are shown as a function of processing speed (v = 0.70 m/min, 0.80 m/min, 0.85 m/min and 0.90 m/min) and oscillation frequency (f = 100 Hz, 500 Hz and 1000 Hz) for different waveform patterns: sinusoidal (SNW), triangular (TNW), square (SQW), ramp-up (RUW), and ramp-down (RDW). The oscillation amplitude was fixed at A = 15 mm. Additionally, the static reference condition is indicated by a grey dashed line, with the adjacent grey area representing its standard deviation.

The static reference condition at a processing speed of 0.70 m/min exhibited a burr height of approximately 2.0 mm. In comparison, axial oscillations yielded operating conditions in which a significant reduction in burr formation occurred, while the processing speed was maintained or even increased. For sinusoidal oscillations, burr heights at f = 1000 Hz were comparable to the static condition and worsened as cutting speed increased for both focal positions. In contrast, oscillations at f

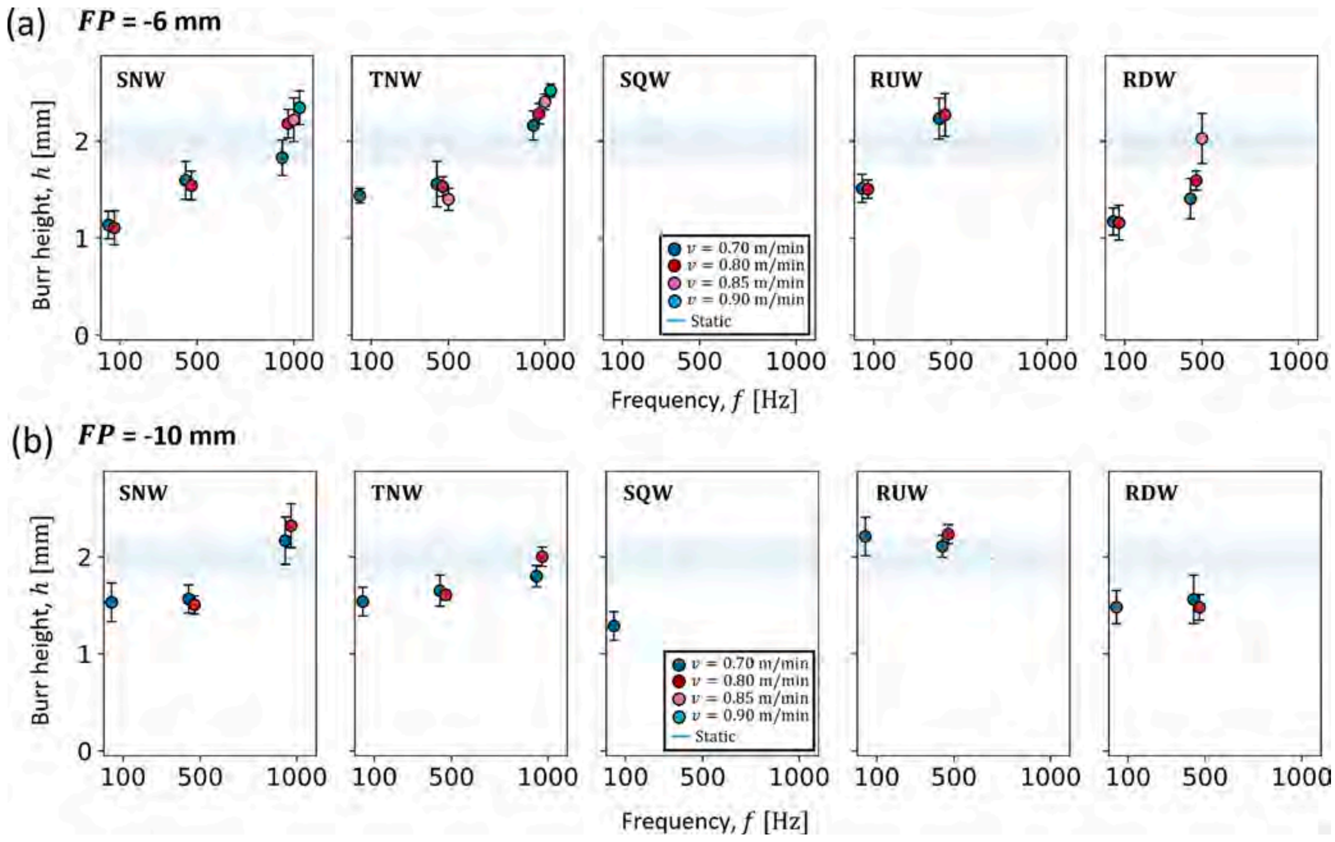

Fig. 10. Burr height retrieved from the microscope image analysis of the 20 mm thick AISI304 stainless steel samples cut-edges for (a) *FP* = -6 mm and (b) *FP* = -10 mm. Different combinations of processing speed (v = 0.70 m/min, 0.80 m/min, 0.85 m/min and 0.90 m/min) and oscillation frequency (f = 100 Hz, 500 Hz and 1000 Hz) for different waveform patterns: sinusoidal (SNW), triangular (TNW), square (SQW), ramp-up (RUW), and ramp-down (RDW). The oscillation amplitude was fixed at A = 15 mm. Mean values and one standard deviation error bars are shown. The static reference condition is indicated by a grey dashed line, with the adjacent grey area representing its standard deviation.

$= 500$ Hz and $f = 100$ Hz consistently yielded burr heights below the reference, with the lowest value of approximately 1.1 mm obtained at $FP = -6$ mm and $f = 100$ Hz for both 0.70 m/min and 0.80 m/min, representing a substantial improvement over the static case. A similar trend was observed for triangular oscillations. At $f = 1000$ Hz, the burr height remained comparable to the static condition, with a noticeable deterioration at higher cutting speeds. In contrast, $f = 500$ Hz and $f = 100$ Hz consistently resulted in reduced burr levels. The minimum burr height, approximately 1.3 mm, was obtained at $FP = -6$ mm for both $f = 100$ Hz and $f = 500$ Hz, regardless of the applied cutting speed. Notably, a burr height of 1.3 mm was also measured at $FP = –6$ mm and $f = 500$ Hz at a significantly higher cutting speed ($v = 0.85$ m/min) compared with the static case. For square oscillations, the only available processing speed produced a burr height of approximately 1.2 mm, significantly lower than the reference case. Finally, for ramp-up and ramp-down waveforms at $FP = -10$ mm, burr heights were respectively slightly above and below the reference. At $FP = -6$ mm, burr values remained comparable to the reference at $f = 500$ Hz, whereas the lowest burr heights were achieved at $f = 100$ Hz, with values of approximately 1.4 mm for ramp-up and 1.2 mm for ramp-down oscillations.

4.3. Discussion

Experimental results demonstrate notable improvements in process performance through dynamic beam shaping via axial oscillation, either by reducing burr and roughness defects at the same cutting speed or by increasing productivity while maintaining equivalent part quality.

The results provided in Fig. 8 clearly indicate that the cutting speed can be significantly increased by applying high-frequency axial oscillations. Only for the square waveforms no significant improvements could be observed (since they maintained a processing speed of 0.70 m/min). By contrast, ramp-up and ramp-down oscillations increased the speed to 0.80 m/min and 0.85 m/min, respectively, at $FP = -6$ mm, $f = 500$ Hz and $A = 15$ mm. The highest values, up to 0.90 m/min compared to 0.70 m/min under static reference conditions, were achieved using sinusoidal and triangular oscillations with a focal position of $FP = -6$ mm, an oscillation frequency of $f = 1000$ Hz, and an amplitude of $A = 15$ mm. These improvements in cutting speed can be attributed to enhanced process efficiency, resulting from a more favourable interaction between the laser radiation and the material when axial oscillations are applied. Simulations of the time-averaged intensity distributions for the different oscillation patterns indicate that axial oscillations substantially modify the effective intensity distribution delivered to the workpiece. In particular, the oscillations reduce the local peak intensity while maintaining a more homogeneous energy delivery over an extended axial range (see section 4.1). This more uniform distribution along the beam propagation direction, is expected to promote a steadier absorption of laser power throughout the material thickness. Such conditions enhance the overall process efficiency and consequently enable higher cutting speeds, as experimentally demonstrated in the present study. In particular, higher oscillation frequencies were shown to support higher cutting speeds. This behaviour is attributed to the ability of high-frequency axial oscillations to generate a more homogeneous intensity distribution compared to low-frequency oscillations, which in turn increases absorptivity and improves cutting performance.

Increases in processing speed were observed for sinusoidal, triangular, and ramps oscillations, all of which maintained a relatively homogeneous time-averaged intensity distribution across the oscillation range. Among these, sinusoidal and triangular oscillations achieved the highest maximum cutting speed of 0.90 m/min, while ramp-down and ramp-up oscillations showed a reduced cutting speed of 0.85 m/min and 0.8 m/min respectively. Although the time-averaged intensity distribution for ramp oscillations is similar in shape to that of sinusoidal and triangular oscillations, the difference in cutting speeds is attributed to the effect of oscillation frequency. Specifically, the maximum cutting speed for sinusoidal and triangular oscillations was achieved at 1000 Hz, a frequency unattainable for ramp oscillations due to the dynamic limitations of the mirror, as described in section 3.2. This highlights the critical role of oscillation frequency in determining process performance. In contrast, square oscillations did not provide significant improvements, likely due to their less homogeneous and more variable time-averaged intensity distribution, which reduced process efficiency and resulted in performance comparable to the static reference condition.

For the selected productivity-oriented conditions, the resulting part quality under dynamic operation was generally lower, or at best comparable, to that achieved under the static reference condition. Specifically, although axial oscillations reduced the cut-edge roughness, this improvement was accompanied by an increase in burr formation. Burr heights reached approximately 2.3 ± 0.3 mm for sinusoidal and triangular oscillations, 2.1 ± 0.2 mm for ramp-up oscillations, and 2.0 ± 0.2 mm for ramp-down oscillations, compared to 2.0 ± 0.2 mm observed in the reference case (see Fig. 10).

Conversely, from both scientific and industrial perspectives, the primary objective is to optimize part quality while maintaining the highest possible processing speed. As previously discussed, burr height and surface roughness are the key indicators commonly used to evaluate part quality in the laser cutting of high-thickness metallic materials. Axial oscillations with different waveform patterns were found to produce only minor variations in surface roughness, while exerting a pronounced influence on burr formation. Therefore, for each oscillation waveform, the samples exhibiting the lowest burr defects, while maintaining or even increasing the cutting rate, were identified. The corresponding process parameters (focal position, cutting speed, oscillation amplitude, and frequency) associated with these selected conditions are summarized in Table 4. Microscope images of the (a) cut-edges and (b) cross-sections obtained under these selected process conditions for each oscillation pattern are shown in Fig. 11. The nominal cutting speed is explicitly reported.

For the selected conditions, part quality was assessed not only through the primary quality indicators (burr height and surface roughness) but also through the kerf geometry, evaluated in terms of the average value and deviation of the kerf width and kerf perpendicularity. The measurement procedures followed the methodology described in section 3.3.1. The part quality results obtained under static and dynamic beam shaping conditions for these selected cases are presented in Fig. 12 for comparison. Specifically, Fig. 12a shows the measured burr height, while Fig. 12b reports the surface roughness evaluated at the upper, central and lower regions of the material thickness. Kerf width and kerf perpendicularity are shown in Fig. 12c and Fig. 12d, respectively. Mean values are shown together with error bars representing one standard deviation.

Under static conditions, a cutting speed of 0.70 m/min was achieved with the focal position set 12 mm below the material surface. The resulting burr height was approximately 2.0 mm, while the cut-edge roughness measured about 0.04 mm at the upper position and increased substantially with depth, reaching about 0.20 mm at the middle position and about 0.27 mm at the lower position. The kerf width was approximately 0.5 mm, and the kerf perpendicularity was about 0.15 mm. Conversely, for dynamic conditions, the roughness at the

Table 4
Laser fusion cutting process parameters for 20 mm thick AISI304 stainless steel under static and dynamic beam shaping conditions. Different axial oscillation patterns: Sinusoidal SNW, Triangular TNW, Square SQW, Ramp-up RUW and Ramp-down RDW.

Oscillation patterns	**Static**	SNW	TNW	SQW	RUW	RDW
Focal position, *FP* [mm]	−12	−6	−6	−10	−6	−6
Oscillation amplitude, *A* [mm]	n.a.	15	15	15	15	15
Oscillation frequency, *f* [Hz]	n.a.	100	500	100	100	100
Cutting speed, *v* [m/min]	0.70	0.80	0.85	0.70	0.80	0.80

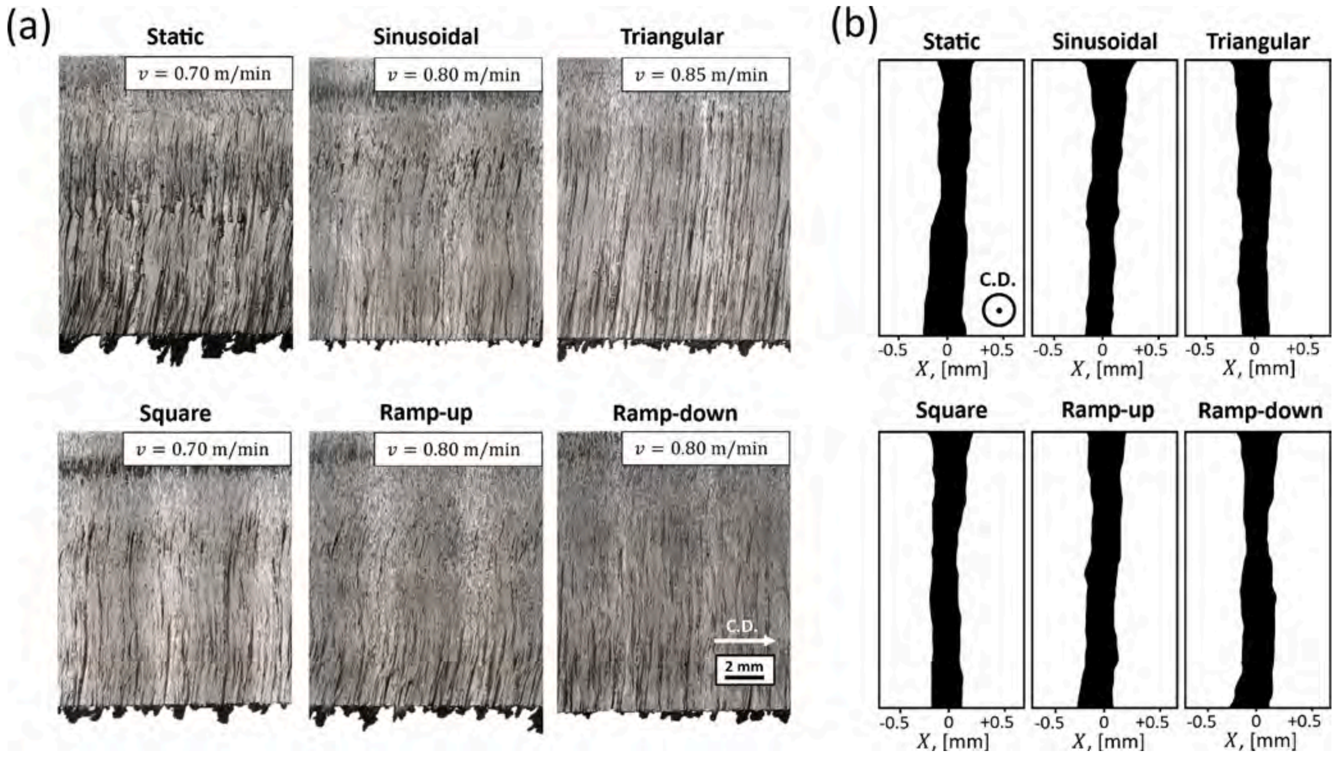

Fig. 11. Microscope images of the (a) cut edges and (b) cross-sections corresponding to the selected process conditions for each axial oscillation waveform. The nominal cutting speed associated with each condition is explicitly indicated.

upper position remained comparable to the static reference for all oscillation waveforms. At the middle and lower positions, the roughness increased relative to the top surface but remained consistently lower than in the static case, with values in the range of 0.05 mm to 0.10 mm at the middle position and 0.10 mm to 0.15 mm at the lower position. The kerf width remained within 0.4 mm − 0.5 mm across all cutting conditions, showing no significant dependence on oscillation pattern. A slight increase in kerf perpendicularity was observed under dynamic conditions compared to the static case, with values around 0.20 mm. While the average kerf width is not significantly affected by axial oscillations, the kerf geometry is strongly influenced by the modified intensity distribution induced by the oscillatory beam motion. Static cutting conditions exhibit a relatively small inlet kerf width that progressively increases toward the bottom of the material thickness. In contrast, the oscillating waveforms produce a larger inlet kerf width that is either maintained or slightly reduced along the thickness. Such an altered kerf geometry is known to facilitate improved coupling of the assist gas into the kerf, thereby enhancing gas flow. This enhanced flow promotes more efficient removal of molten material, ultimately leading to improved cut quality, as also reported by Thomas *et al.* [56].

In addition, cutting front geometry was extracted from microscope images of the sample cross-sections taken longitudinally with respect to the cutting direction, as shown in Fig. 13a for the selected different axial oscillation patterns. A first qualitative inspection of the cut samples indicated that dynamic beam shaping via axial oscillations has only a minor influence on the overall cutting front geometry. However, direct visual comparison across processing conditions is limited; therefore, the cutting front inclination angle was quantitatively evaluated, as reported in Fig. 13b. The measured cutting front incident angles range between 86° and 89°. The static condition and the square waveform exhibit slightly higher incident angles compared to sinusoidal, triangular, ramp-up, and ramp-down oscillations. These results are consistent with the discussion by Mahrle *et al.* [52], who reported that lower cutting front incident angles are expected to enhance the absorptivity coefficient, thereby positively affecting overall process efficiency and enabling higher cutting speeds. In the present study, the more homogeneous intensity distributions associated with sinusoidal, triangular, ramp-up, and ramp-down oscillations lead to a slight reduction in the cutting front incident angle, which correlates with the marginally higher cutting speeds observed under these conditions.

While no significant variations in the roughness profile and only slight variations in kerf and cutting front geometry were observed across the different process conditions or oscillation patterns, a notable reduction in burr formation was achieved under all dynamic beam-shaping strategies. When applying sinusoidal axial oscillations, the burr height was reduced to 1.1 mm, accompanied by a slight increase in cutting speed to 0.80 m/min. This condition corresponded to a focal position oscillating around 6 mm below the upper material surface, with an amplitude of $A = 15$ mm and frequency $f = 100$ Hz. The same processing speed of 0.80 m/min was also achieved with ramp-up and ramp-down waveforms at identical amplitude, frequency and focal position, although the burr height differed slightly: approximately 1.5 mm for ramp-up oscillations and 1.2 mm for ramp-down. Triangular oscillations provided further improvements in processing speed, reaching up to 0.85 m/min. However, the burr height was slightly higher than in the sinusoidal case, though still significantly lower than under static conditions. These results were obtained with a focal position oscillating around 6 mm below the surface, an amplitude of $A = 15$ mm, and a frequency of $f = 500$ Hz. In contrast, square-wave oscillations did not provide benefits in terms of productivity. A cutting speed of 0.70 m/min, equivalent to the static reference, was recorded with a focal position centered at 10 mm below the surface, an amplitude of $A = 15$ mm, and a frequency of $f = 100$ Hz. In this case, the burr height was reduced to 1.2 mm.

Finally, the thermal impact of the process was evaluated through measurements of the heat-affected zone (HAZ). The measurement procedure followed the methodology described in section 3.3.1. Fig. 14a shows an image of the polished sample cross-section taken transverse to the cutting direction, while the corresponding microstructures obtained after chemical etching are reported for three different sections along the sample thickness. The geometry of the heat-affected-zone was

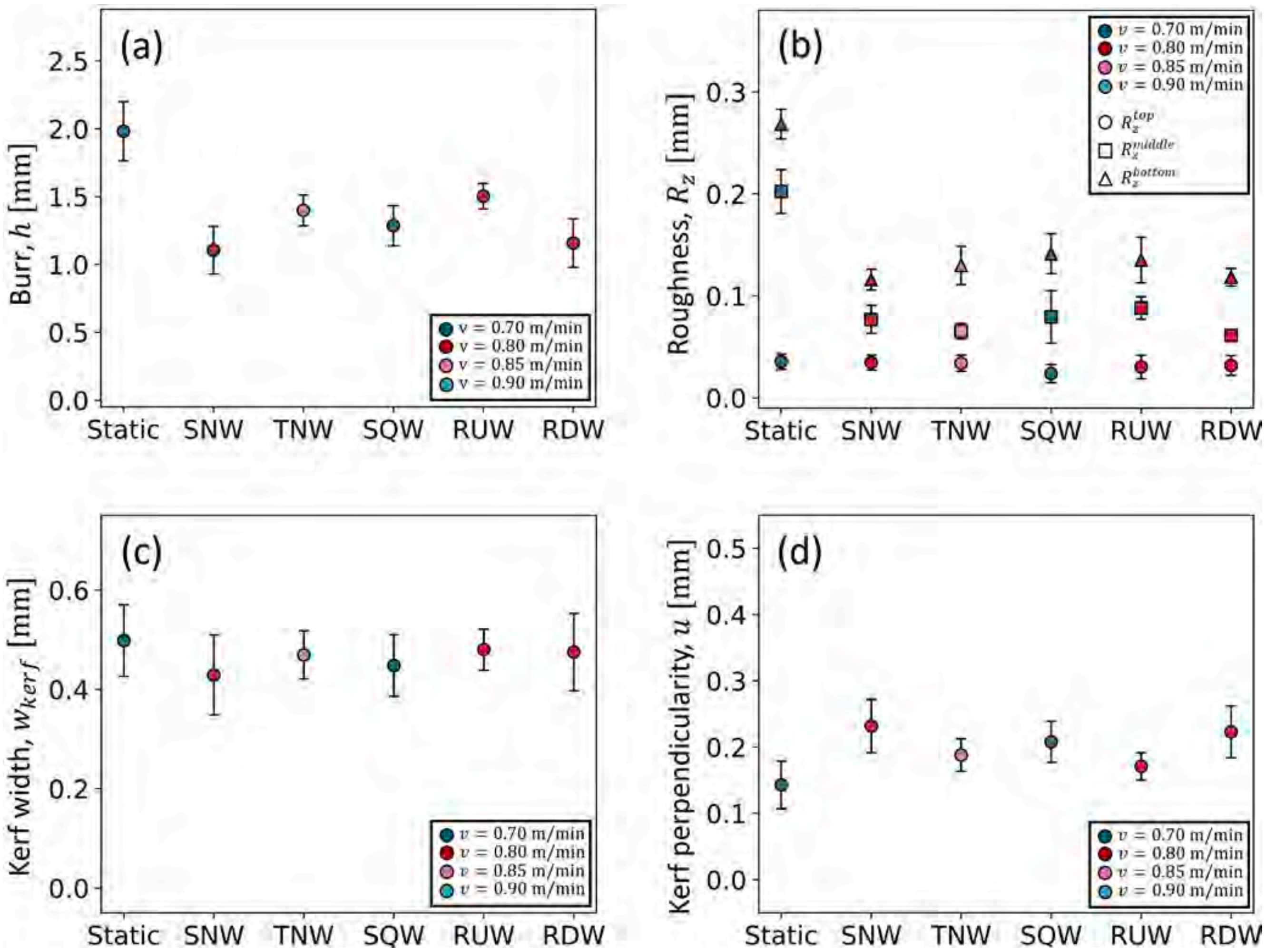

Fig. 12. Part quality for the selected process conditions of 20 mm thick stainless steel AISI304. Different oscillation patterns: Sinusoidal SNW, Triangular TNW, Square SQW, Ramp-up RUW and Ramp-down RDW. The figure reports: (a) burr height; (b) roughness profile measured at the top, middle and bottom positions along the material thickness; (c) average kerf width and its deviation; and (d) kerf perpendicularity. Mean values are shown, with error bars representing three standard deviations.

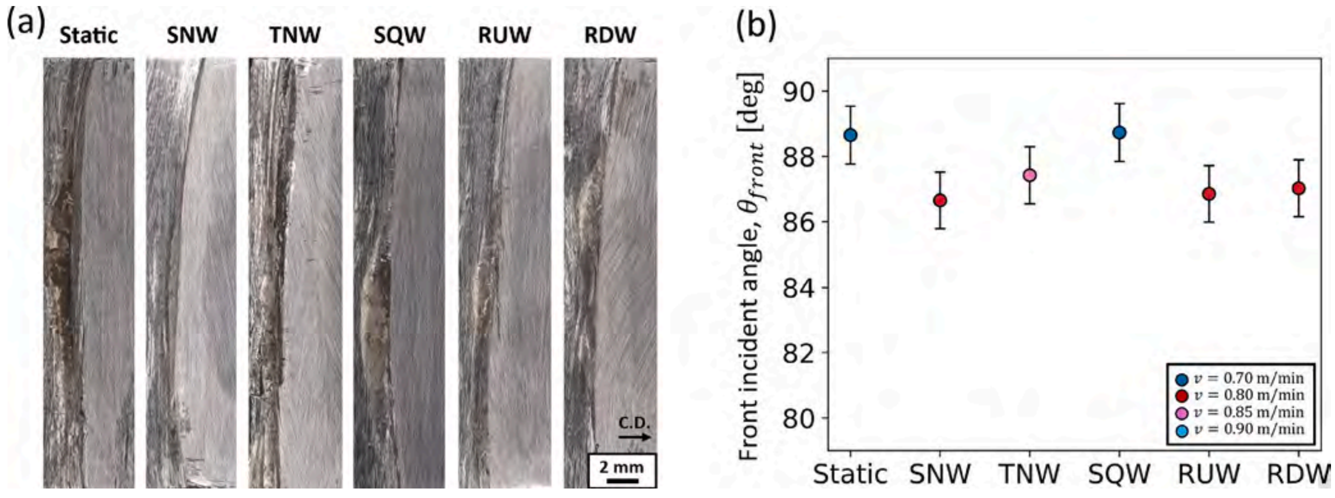

Fig. 13. (a) Microscope images of the sample cross-sections taken longitudinally with respect to the cutting direction and (b) cutting front inclination angle for the selected different axial oscillation patterns.

systematically quantified by measuring its width at multiple locations along the cut edge, equally spaced at 2 mm intervals along the material thickness, resulting in a total of eleven measurement positions, as reported in Fig. 14e.

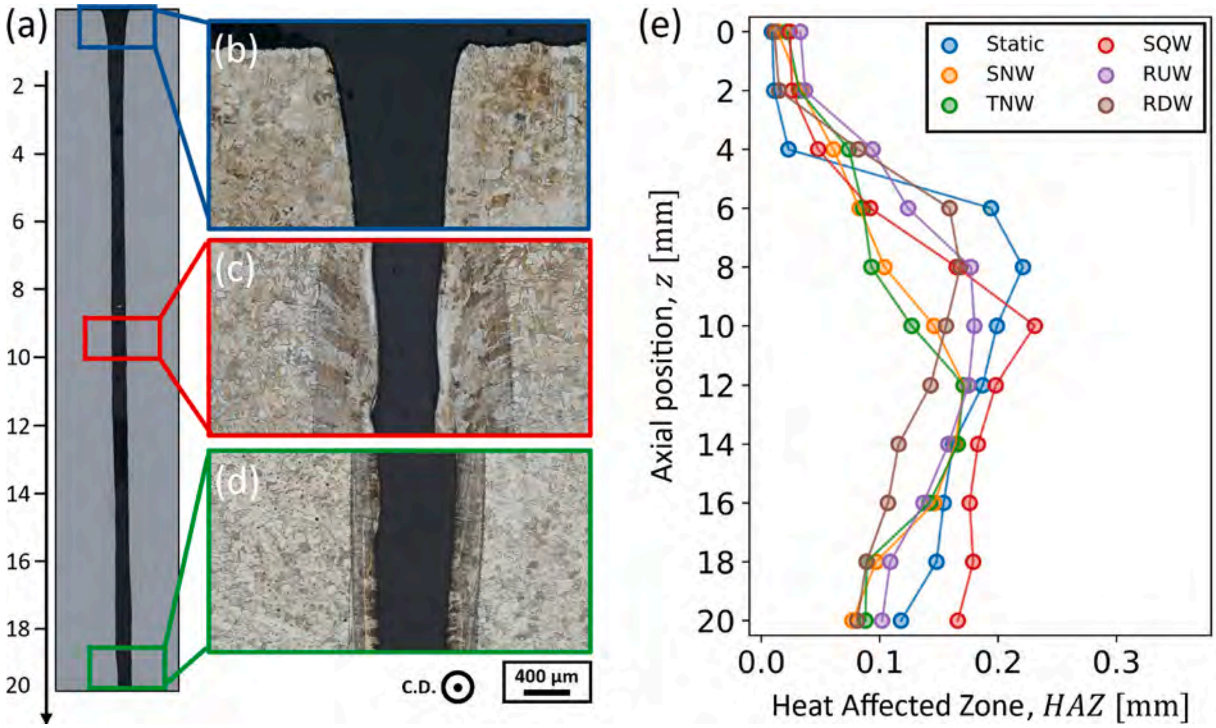

Fig. 14. (a) Optical microscope image of the polished sample cross-section acquired transverse to the cutting direction. (b–d) Optical micrographs of the etched microstructure at three representative locations along the sample thickness. (e) Heat-affected zone (HAZ) width measured at multiple locations along the cut edge for the different oscillation patterns.

From the optical micrographs reported in Fig. 14, the heat-affected zone (HAZ) is clearly distinguishable as the region adjacent to the cutting kerf where the microstructural features deviate from those of the base material. In this region, the grains exhibit a marked increase in size and a pronounced elongation oriented transverse to the cutting kerf, indicating localized thermal exposure and microstructural evolution induced by the laser cutting process. In contrast, the base material retains an equiaxed grain morphology characteristic of the unaffected bulk material. Moreover, a consistent trend in the HAZ distribution is observed for all oscillation waveform conditions. The HAZ is minimal, and in some cases nearly negligible, near the upper surface of the material. Its width progressively increases with depth, reaching a maximum approximately at mid-thickness, before slightly decreasing toward the bottom surface of the sample. Nevertheless, the HAZ in the lower region remains non-negligible and consistently larger than that measured near the upper surface. This behaviour is observed for all oscillation patterns; however, sinusoidal, triangular, ramp-up, and ramp-down oscillations that produce a more homogeneous intensity distribution exhibit a lower maximum HAZ width compared to the other conditions. In addition, these patterns result in a slightly more uniform HAZ along the material thickness, with reduced variation in the measured HAZ relative to the other oscillation modes.

Overall, the experimental results demonstrate that these dynamic beam shaping strategies may led to a significant reduction in burr formation and roughness profile compared to the static reference condition, while simultaneously enabling higher processing speeds. Simulations of the time-averaged intensity distributions for different oscillation patterns revealed that axial oscillations substantially modify the intensity profile within the workpiece. This modified geometry enables better control of the interaction zone between the laser radiation and the material, thereby increasing process absorptivity and leading to higher cutting speeds. In addition, it enhances the coupling of the assist gas into the kerf, promoting more efficient removal of molten material. As a result, cut quality is improved, as experimentally confirmed in the present study. Moreover, although the effect of frequency is not captured by the time-averaged intensity distributions presented in section 4.1, the present study demonstrates that it strongly influences both productivity and part quality. Specifically, low oscillation frequencies promote the most efficient melt ejection, resulting in minimal burr formation at high amplitudes while still increasing cutting speed due to the enhanced process efficiency associated with a more homogeneous intensity distribution. This observation is consistent with previous study by Borkmann *et al.* [55] reporting that specific oscillation frequencies can improve cut quality without necessarily requiring very high frequencies. This behaviour is likely due to the role of axial oscillations in actively assisting the expulsion of molten material from the kerf. Controlled beam movement along the propagation direction at an appropriate oscillation frequency improves melt flow dynamics, enabling more efficient melt ejection compared with static or quasi-static conditions. In contrast, higher frequencies reduce melt removal efficiency and increase burr formation, but produce an even more uniform intensity profile, which enhances absorptivity and improves overall process productivity by enabling significantly higher cutting speeds.

5. Conclusions

The present work explores the impact of various axial oscillation waveforms, namely sinusoidal (SNW), triangular (TNW), square (SQW), ramp-up (RUW), and ramp-down (RDW) patterns, on the laser fusion cutting process through analytical modelling and experimental investigations.

The main outcomes and original contributions of the work can be listed as follows:

- An analytical model was developed, for the first time, to evaluate the laser intensity distribution within the process zone for different axial oscillation waveforms beyond the conventional sinusoidal pattern. Simulations revealed that axial oscillations substantially influence both intensity distribution and shape geometry, leading to a more homogeneous profile along the beam propagation direction and extended Rayleigh length.

- The effect of axial oscillations superimposed on the cutting direction was experimentally investigated in the processing of 20 mm thick AISI304 stainless steel. Experimental results demonstrate notable improvements in process performance through axial oscillation, either by reducing burr height and roughness profile defects at the same processing speed or by increasing productivity while maintaining equivalent part quality.
- Specifically, while employing square waveform axial oscillation improves part quality at the same processing speed as the reference static condition, all other waveform patterns yield significant improvements in both part quality and processing speed. The best process performances were obtained using sinusoidal and triangular axial oscillations.
- The experimental results are consistent with theoretical findings. A more homogeneous intensity profile promotes more uniform laser absorption across the material thickness, enhancing process efficiency and enabling higher cutting speeds. In parallel, the altered intensity profile influence kerf geometry and may improve assistant gas coupling and molten material removal, which ultimately benefits cut quality. In addition, the oscillation frequency has been shown to play a crucial role in process performance, as it actively assists in expelling molten material from the kerf. Among the tested patterns, triangular oscillations yielded slightly better performance than sinusoidal oscillations, likely due to the more uniform intensity distribution resulting from the absence of inversion points.

While this study provided a first methodological investigation into the effect of different axial oscillation patterns on process productivity and part quality through experimental analysis and analytical modelling, future work will focus on a more in-depth analysis of the underlying mechanisms. In particular, these studies will aim to better understand how oscillation motion affects the microscopic interaction between laser radiation and the material, with a focus on the influence of oscillation amplitude and frequency on workpiece temperature and melt flow dynamics. This will be pursued through thermal monitoring and high-speed imaging of the cutting process to capture and evaluate transient process phenomena. Additionally, future work will target specific oscillation patterns to quantitatively validate qualitative insights from the modelling. In particular, the direct relationship between the dynamic laser beam intensity profile, process efficiency, and kerf geometry will be examined for sinusoidal oscillations, which demonstrated the most promising results in terms of both increased cutting speed and reduced burr formation.

CRediT authorship contribution statement

Matteo Busatto: Writing – review & editing, Writing – original draft, Visualization, Validation, Methodology, Investigation, Conceptualization. **Julia Meyer:** Supervision, Resources, Investigation. **Leonardo Caprio:** Writing – review & editing, Supervision, Project administration, Conceptualization. **Davide Gandolfi:** Writing – review & editing, Supervision, Project administration, Conceptualization. **Barbara Previtali:** Writing – review & editing, Supervision, Resources, Project administration.

Declaration of competing interest

The authors declare that they have no known competing financial interests or personal relationships that could have appeared to influence the work reported in this paper.

Acknowledgements

The authors gratefully acknowledge the Italian Ministry for University and Research (MUR) for supporting the research via the National Plan for Recovery and Resilience (PNRR).

References

[1] Davim JP, editor. Nontraditional Machining Processes: Research Advances [Internet]. London: Springer London; 2013 [cited 2023 Oct 5]. Available from: https://link.springer.com/10.1007/978-1-4471-5179-1.
[2] C.L. Caristan, Laser cutting guide for manufacturing, Society of Manufacturing Engineers (2003).
[3] S. Genna, E. Menna, G. Rubino, V. Tagliaferri, Experimental Investigation of Industrial Laser cutting: the effect of the material selection and the process parameters on the kerf quality, Appl. Sci. 10 (14) (2020) 4956.
[4] M. Sharifi, M. Akbari, Experimental investigation of the effect of process parameters on cutting region temperature and cutting edge quality in laser cutting of AL6061T6 alloy, Optik 184 (2019) 457–463.
[5] M. Schmidt, K. Cvecek, J. Duflou, F. Vollertsen, C.B. Arnold, M.J. Matthews, Dynamic beam shaping—Improving laser materials processing via feature synchronous energy coupling, CIRP Ann. (2024).
[6] Pocorni JK, Petring D, Powell J, Deichsel E, Kaplan AFH. Differences in cutting efficiency between CO2 and fiber lasers when cutting mild and stainless steels. In: International Congress on Applications of Lasers & Electro-Optics [Internet]. San Diego, California, USA: Laser Institute of America; 2014 [cited 2024 July 22]. p. 593–600. Available from: http://aip.scitation.org/doi/abs/10.2351/1.5063108.
[7] Bohdal Ł, D. Schmidtke. Effect of fiber and CO2 lasers parameters on the cut surface quality of RVS 1.4301 stainless steel. JMES. 2022 June 30;16(2):8862–72.
[8] G.C. Rodrigues, J.R. Duflou, Into the development of a model to assess beam shaping and polarization control effects on laser cutting, J. Phys. D Appl. Phys. 51 (6) (2018) 065601.
[9] G.C. Rodrigues, J.R. Duflou, Effects of different polarization strategies on laser cutting with direct diode lasers, Phys. Procedia 83 (2016) 302–309.
[10] A.H.A. Lutey, A. Ascari, A. Fortunato, L. Romoli, Long-pulse quasi-CW laser cutting of metals, Int. J. Adv. Manuf. Technol. 94 (1–4) (2018) 155–162.
[11] A.F.M. Tahir, S.N. Aqida, An investigation of laser cutting quality of 22MnB5 ultra high strength steel using response surface methodology, Opt. Laser Technol. 92 (2017) 142–149.
[12] K. Fuse, Beam Shaping for Advanced Laser Materials Processing: Generation of shape and intensity profile of laser beam with aspheric and diffractive optics, Laser Tech. J. 12 (2) (2015) 19–22.
[13] D.A.V. Kliner, B. Victor, A Breakthrough for Fiber Lasers: Tunable beam quality enables optimized cutting of thin and thick metal, PhotonicsViews 16 (1) (2019) 51–55.
[14] M. Busatto, L. Caprio, B. Previtali, Investigating the effect of dynamic laser beam oscillations in remote fusion cutting process, J. Laser Appl. 36 (4) (2024) 042068.
[15] S. D'Arcangelo, M. Busatto, L. Caprio, B. Previtali, A.G. Demir, Hybrid use of a robotic welding system in remote laser separation of thin-sheet Al casings for the recycling of battery packs, J. Laser Appl. 36 (3) (2024) 032023.
[16] C. Goppold, T. Pinder, P. Herwig, A. Mahrle, A. Wetzig, E. Beyer, Beam oscillation – periodic modification of the geometrical beam properties. Proceedings of the International Conference on Lasers in Manufacturing [internet], 2015. Available from: https://www.wlt.de/lim/Proceedings/Stick/PDF/Contribution112_final.pdf.
[17] C. Goppold, T. Pinder, P. Herwig, Transient beam oscillation with a highly dynamic scanner for laser beam fusion cutting, Advanced Optical Technologies. 5 (1) (2016) 61–70.
[18] C. Goppold, P. Herwig, D. Stoffel, M. Bach, Tip-tilt piezo platform scanner qualifies dynamic beam shaping for high laser power in cutting applications. Proceedings of the International Conference on Lasers in Manufacturing [internet], 2019. Available from: https://wlt.de/lim/Proceedings2019/data/PDF/Contribution_172_final.pdf.
[19] N. Levichev, M.R. Vetrano, J.R. Duflou, Melt flow and cutting front evolution during laser cutting with dynamic beam shaping, Opt. Lasers Eng. 161 (2023) 107333.
[20] N. Levichev, P. Herwig, A. Wetzig, J.R. Duflou, Towards robust dynamic beam shaping for laser cutting applications, Procedia CIRP 111 (2022) 746–749.
[21] M. Kardan, N. Levichev, S. Castagne, J.R. Duflou, Cutting thick aluminum plates using laser fusion cutting enhanced by dynamic beam shaping, J. Laser Appl. 35 (4) (2023) 042074.
[22] M. Kardan, N. Levichev, J.R. Duflou, Experimental and numerical investigation of thick plate laser cutting using dynamic beam shaping, Procedia CIRP 111 (2022) 740–745.
[23] A. Gropp, J. Hutfless, S. Schuberth, M. Geiger, Laser beam cutting, Opt. Quant. Electron. 27 (12) (1995) 1257–1271.
[24] T. Okada, K. Ebata, M. Shiozaki, T. Kyotani, A. Tsuboi, M. Sawada, et al., Development of adaptive mirror for CO2 laser, Proc. SPIE-Int. Soc. Opt. Eng. 1 (2000).
[25] D. He, T. Shinshi, T. Nakai, Development of a maglev lens driving actuator for off-axis control and adjustment of the focal point in laser beam machining, Precis. Eng. 37 (2) (2013) 255–264.
[26] Y. Morimoto, D. He, W. Hijikata, T. Shinshi, T. Nakai, N. Nakamura, Effect of high-frequency orbital and vertical oscillations of the laser focus position on the quality of the cut surface in a thick plate by laser beam machining, Precis. Eng. 40 (2015) 112–123.
[27] P. Böttner, C. Reinlein, A. Jahn, P. Herwig, C. Goppold, D. Stoffel, et al., Design, manufacturing and test of a highly dynamic piezo- driven metal mirror for laser material processing. Proceedings of the International Conference on Lasers in

Manufacturing [internet], 2019. Available from: https://www.wlt.de/lim/Proceedings2019/data/PDF/Contribution_294_final.pdf.
[28] A. Jahn, C. Goppold, P. Herwig, C. Reinlein, P. Boettner, D. Stoffel, et al., High dynamic beam shaping by piezo driven modules for efficient and high quality laser beam cutting and welding. Proceedings of the International Conference on Lasers in Manufacturing [internet], 2019. Available from: https://www.wlt.de/lim/Proceedings2019/data/PDF/Contribution_285_final.pdf.
[29] P. Herwig, Laser Sawing with piezo-driven adaptive mirror, The Laser User (2021).
[30] Mahrle A, Beyer E. Modeling and simulation of the energy deposition in laser beam welding with oscillatory beam deflection. In: International Congress on Applications of Lasers & Electro-Optics [Internet]. Orlando, Florida, USA: Laser Institute of America; 2007 [cited 2023 Nov 27]. p. 1805. Available from: http://aip.scitation.org/doi/abs/10.2351/1.5061037.
[31] T. Girerd, A. Gameros, M. Simonelli, A. Norton, A.T. Clare, Modulation of melt pool behaviour using novel laser beam oscillation methods, J. Mater. Process. Technol. 325 (2024) 118300.
[32] C. Zhang, X. Li, M. Gao, Effects of circular oscillating beam on heat transfer and melt flow of laser melting pool, J. Mater. Res. Technol. 9 (4) (2020) 9271–9282.
[33] T. Girerd, A.G. Madrigal, A. Clare, A. Norton, Lissajous curve oscillations in laser welding, Procedia CIRP 111 (2022) 562–565.
[34] Serov V. Fourier Series, Fourier Transform and Their Applications to Mathematical Physics [Internet]. Cham: Springer International Publishing; 2017 [cited 2025 Sept 3]. (Applied Mathematical Sciences; vol. 197). Available from: http://link.springer.com/10.1007/978-3-319-65262-7.
[35] The British Standards Institution. BS EN 10088-3:2023 - TC Stainless steels - Technical delivery conditions for semi-finished products, bars, rods, wire, sections and bright products of corrosion resistant steels for general purposes. BSI Standards Limited 2024; 2024.
[36] Steen WM, Mazumder J. Laser Material Processing [Internet]. London: Springer London; 2010 [cited 2023 Oct 5]. Available from: http://link.springer.com/10.1007/978-1-84996-062-5.
[37] Reinlein C, Ulrich S, Kühl P, Bach J, Lübke F, Fischer M, et al. Blue Modern Scientific Poster (84 × 118.8 cm)-3. 2023 [cited 2023 Sept 5]; Available from: https://rgdoi.net/10.13140/RG.2.2.33240.57606.
[38] O. Bocksrocker, P. Berger, B. Regaard, V. Rominger, T. Graf, Characterization of the melt flow direction and cut front geometry in oxygen cutting with a solid state laser, J. Laser Appl. 29 (2) (2017) 022202.
[39] E. Fallahi Sichani, S. Kohl, J.R. Duflou, Plasma detection and control requirements for CO 2 laser cutting, CIRP Ann. 62 (1) (2013) 215–218.
[40] M. Pacher, S. Strada, M. Tanelli, B. Previtali, S.M. Savaresi, Real-time velocity regulation for productivity optimization in laser cutting, IFAC-PapersOnLine 54 (1) (2021) 1230–1235.
[41] M. Pacher, L. Monguzzi, L. Bortolotti, M. Sbetti, B. Previtali, Quantitative identification of laser cutting quality relying on visual information. Proceedings of the International Conference on Lasers in Manufacturing, 2017.
[42] M. Pacher, L. Franceschetti, S.C. Strada, M. Tanelli, S.M. Savaresi, B. Previtali, Real-time continuous estimation of dross attachment in the laser cutting process based on process emission images, J. Laser Appl. 32 (4) (2020) 042016.
[43] M. Pacher, L. Caprio, G. Delama, D. Gandolfi, M. Savaresi, B. Previtali, et al., Real-time roughness estimation in laser oxidation cutting via coaxial process vision. Proceedings of the International Conference on Lasers in Manufacturing [internet], 2023. Available from:.
[44] Miloš MADIĆ, Constantin Cristinel GIRDU, Dragan MARINKOVIĆ, Predrag JANKOVIĆ, Milan TRIFUNOVIĆ. Analysis of Kerf Width and its Variation in CO2 Laser Cutting of Straight and Curved Cut Profiles. Teh vjesn [Internet]. 2024 Dec 15 [cited 2025 Aug 5];31(6). Available from: https://hrcak.srce.hr/321909.
[45] J. Lind, F. Fetzer, D. Blazquez-Sanchez, J. Weidensdörfer, R. Weber, T. Graf, Geometry and absorptance of the cutting fronts during laser beam cutting, J. Laser Appl. 32 (3) (2020) 032015.
[46] C. Goppold, T. Pinder, S. Schulze, P. Herwig, A.F. Lasagni, Improvement of laser beam fusion cutting of mild and stainless steel due to longitudinal, linear beam oscillation, Appl. Sci. 10 (9) (2020) 3052.
[47] Technical Commitee ISO/TC 213. ISO 21920-2:2021 - Geometrical product specifications - Surface texture. 2021.
[48] Technical Comitee ISO/TC 44. EN ISO 9013:2017 - Thermal cutting - Classification of thermal cuts - Geometrical product specification and quality tolerances. 2017.
[49] L. Caprio, A.G. Demir, B. Previtali, Understanding the effects of temporal waveform modulation of laser emission power in laser powder bed fusion: Part II - Experimental investigation, J. Phys. D Appl. Phys. 55 (49) (2022) 495110.
[50] S.E. Nielsen, N. Ellis, Dual-focus laser cutting, Weld. World 46 (3–4) (2002) 33–40.
[51] J. Volpp, Laser process manipulation by axial beam shaping, Lasers in Manufacturing Conference. (2021).
[52] A. Mahrle, E. Beyer, Theoretical aspects of fibre laser cutting, J. Phys. D Appl. Phys. 42 (17) (2009).
[53] Mahrle A, Bartels F, Beyer E. Theoretical aspects of the process efficiency in laser beam cutting with fiber lasers. In: International Congress on Applications of Lasers & Electro-Optics [Internet]. Temecula, California, USA: Laser Institute of America; 2008 [cited 2023 Sept 5]. p. 2006. Available from: http://aip.scitation.org/doi/abs/10.2351/1.5061285.
[54] J. Lind, C. Hagenlocher, N. Weckenmann, D. Blazquez-Sanchez, R. Weber, T. Graf, Adjustment of the geometries of the cutting front and the kerf by means of beam shaping to maximize the speed of laser cutting, Int. J. Adv. Manuf. Technol. 126 (3–4) (2023) 1527–1538.
[55] M. Borkmann, A. Mahrle, P. Herwig, A. Wetzig, Fundamental characteristics of fiber laser beam sawing of 10 mm thick stainless steel. Proceedings of the International Conference on Lasers in Manufacturing [internet], 2021. Available from:.
[56] Thomas S, Powell J, Speker N, Hesse T, Hagenlocher C, Graf T. Influence of the kerf geometry on the flow field and the transfer of kinetic energy to the melt during laser fusion cutting as a function of cutting speed. Int J Adv Manuf Technol [Internet]. 2025 Nov 1 [cited 2025 Nov 10]; Available from: https://link.springer.com/10.1007/s00170-025-16899-5.